SMALL ANGLE SCATTERING OF METASTABLE HYDROGEN FORMED BY COLLISIONAL EXCITATION OF NEUTRAL HYDROGEN

A THESIS

Presented to

The Faculty of the Division of Graduate

Studies and Research

By

Isidor Sauers

In Partial Fulfillment

of the Requirements for the Degree

Doctor of Philosophy

in the School of Physics

Georgia Institute of Technology

June, 1974

SMALL ANGLE SCATTERING OF METASTABLE HYDROGEN FORMED

BY COLLISIONAL EXCITATION OF NEUTRAL HYDROGEN

Approved:

E. W. Thomas, Chairman

M. R. Flannery

T. F. Moran

Date approved by Chairman: 10 May 1974

ACKNOWLEDGMENTS

It is with sincere gratitude that I acknowledge the help of those who have contributed to the research described in this dissertation. I wish to thank Dr. T. F. Moran and Dr. M. R. Flannery, who served on my reading committee and offered helpful suggestions on the manuscript. In addition, Dr. Flannery was instrumental in the development of portions of the theoretical portion of this thesis.

Dr. R. L. Fitzwilson provided valuable guidance in the early stages of my experimental work. To Dr. J. C. Ford I am particularly grateful for supplying useful advice on the design of various components of the vacuum system utilized in the present research. Messrs. K. B. Springfield and J. R. Bell were responsible for the fabrication of many of these components. I must also acknowledge the aid of Mr. Wayne Hill for his assistance in the operation of the experiment. The excellent typing of the final draft of this manuscript is credited to Mrs. Carolyn Piersma.

It is impossible to overstate the influence of my thesis advisor, Dr. E. W. Thomas, on the total research program from initiation to completion. He satisfied both the role of experimentalist and teacher in guiding my research. The continued confidence that he expressed in my work was most appreciated. His excellence in and flair for experimental research has provided a high standard which I hope to achieve in my future research.

Finally, I must express my deepest gratitude to my parents,

who provided encouragement throughout my educational career. None of this work would have been possible without their ever-present faith and patience.

TABLE OF CONTENTS

LIST OF TABLES

LIST OF ILLUSTRATIONS

Figure Page

SUMMARY

An experimental investigation of collisional excitation in neutral-neutral collisions has been made. Total cross sections for the process represented by

$$H(1s) + X \rightarrow H(2s) + X \ , \qquad (1)$$

where X is either helium or argon, were measured for impact energies ranging from 1-20 keV. Differential (in angle) cross sections, for process (1) for a helium target, were measured in the angular range 0.2°-1.5° at 1.5, 5.0, 10.0, 15.0, and 20.0 keV impact energies. Also, measurement of the differential cross section for

$$H(1s) + He \rightarrow H^{o} + He \qquad (2)$$

and

$$H(1s) + He \rightarrow H^{+} + e + He \ , \qquad (3)$$

where (2) includes scattered hydrogen formed in any bound state and (3) includes hydrogen excited to any continuum state, were made at 10 keV.

The objective was to test various theoretical approximations (Born approximation, multistate impact parameter approximation, and distorted wave Born Eikonal approximation); to this end differential as well as total cross sections were required to provide a sensitive determination of the range of validity of the theories.

The experimental arrangement used for the measurement of all

three processes consisted of an ion source and accelerator to provide fast protons; a differentially pumped gas cell through which the protons passed, resulting in formation of fast hydrogen atoms; field removal of ions and metastable hydrogen atoms from the primary beam; a cell containing a gaseous target; and detectors for measuring H(2s), H^o, and H^+ scattered fluxes. The detection of H(2s) was by field induced emission of 1216 Å photons, using a channel electron multiplier for photon detection. At scattering angles below 1.5°, proton currents were measured directly by a conventional Faraday cup, while neutral hydrogen atoms were measured by detection of secondary electrons, ejected from a metal surface, resulting from hydrogen atom impact; for larger scattering angles, H^+ and H^o were detected as single particles by channel electron multipliers. For total cross section measurements (process (1)), angle defining apertures utilized in the measurement of differential cross sections were removed. The analysis of the small angle scattering data, with regard to the distorting effects due to the finite angular resolving power, is also investigated.

When possible, comparison is made with theoretical predictions. Good agreement is found with the Born approximation for total cross sections down to 10 keV; however differential cross sections disagree by many orders of magnitude. Predictions of the multistate impact parameter approximation for total cross sections agree with the data down to 4.0 keV. Differential cross sections predicted by the distorted wave Born Eikonal approximation and multistate impact parameter approximation agree with experiment in angular dependence, but differ in magnitude by a factor of four. Measurement of the angular

distribution for (1) at 1.5 keV show structure which is in accord with theoretical predictions.

CHAPTER I

INTRODUCTION

The study of collisions between heavy particles has proven to be a useful approach to the understanding of atomic structure. In the past, research in heavy particle collisions have been almost totally relegated to ion-atom collisions, primarily due to the inherent practicality of firing a beam of ions into a gaseous target. This "advantage" to the experimentalist becomes a "disadvantage" to the theoretician because of the difficulty in solving Schroedinger's equation with potentials that are long range. A critique of the research in the past twenty-five years of excitation due to collisions between heavy particles is given by Thomas.[1] Almost all of the work has involved ion-atom collisions.

Much of the earlier work in collisional excitation due to neutral-neutral encounters[5] has been in the measurement of ionization cross sections;[2,3,4] but for the purpose of testing theoretical models, collisions resulting in excitation of one of the colliding systems to a particular bound state offer more information. Since the wave functions of hydrogen are well known, the collision between hydrogen atoms is the most theoretically tractable. Hydrogen-hydrogen collisions, however, have numerous experimental difficulties associated with their measurement. Collisions involving a hydrogen projectile and a helium target are simpler to perform experimentally

while still yielding data which can be compared to theoretical predictions.

In the present work collisions resulting in excitation of hydrogen to the first excited state were studied. This is represented by the process

$$H(1s) + X \rightarrow H(2s) + X \qquad (1)$$

where X represents targets of helium or argon. Prior to this work, only total cross sections for this collision process have been studied by Ankudinov *et al.*,[5] Orbeli *et al.*,[6] Birely and McNeal,[7] and Hughes and Choe.[8] Total cross sections for formation of other excited states of hydrogen have been measured by Birely and McNeal[7] and Dose *et al.*[9] (excitation of hydrogen to the 2p state), and Hughes *et al.*[10] (excitation of hydrogen to the 3ℓ states). Much of this past work was motivated by an interest in studying upper atmospheric phenomena, particularly with regard to hydrogen collisions in auroras. The range of applicability for process (1) has also been extended to the controlled thermonuclear research program in which information is needed on the production of neutral hydrogen beams for injection into the plasma and information is required on excitation of the hydrogen atoms after undergoing further collisions.

Theoretical investigations of the collision in Equation (1) have proceeded during this same period of time. Bates[11,12] applied the Born approximation for various collisions involving hydrogen atoms and in 1969 Levy[13,14] and Flannery[15,16,17] performed the Born approximation and multistate impact parameter approximation to hydrogen-hydrogen and

hydrogen-helium collisions. Experimental measurements were thus made in an energy range (1-20 keV) so as to assess the accuracy of these theories. Unfortunately the measurement of total cross sections is insufficient to unambiguously investigate the theoretical accuracy since the theoretical prediction of differential (in angle) cross sections (which is summed over all angles to produce total cross sections) may be in complete disagreement with experiment whereas the total cross sections agree; an example of this will be shown in Chapter VI. Thus differential cross sections for process (1) have been measured over a limited angular range (0.2°-1.5°) to sensitively test the Born approximation, multistate approximations, and the recently developed distorted wave Born Eikonal approximation.[18,19]

Differential cross sections were also measured for the collisional processes

$$H(1s) + He \rightarrow H^{o} + He \qquad (2)$$

and

$$H(1s) + He \rightarrow H^{+} + e + He \quad . \qquad (3)$$

Equation (2) includes scattered hydrogen in the ground (elastically scattered) and hydrogen excited to any bound state; Equation (3) includes excitation of hydrogen to any unbound state (ionization). No previous measurement of the differential cross sections for (1), (2), and (3) have been made. For (2) and (3) comparison with classical predictions will be made.

The measurement of total and differential cross sections for process (1) were made by the detection of field induced photon emission of the long lived 2s state, which is formed in the collision.

Collisions (2) and (3) were studied using current measuring and particle counting techniques. The details of the experimental arrangement and detection methods will be discussed in Chapters II and III respectively. The differential cross sections are defined in terms of the measurable parameters and the apparatus resolution is discussed in Appendix B. Since some of the data was taken at scattering angles comparable in magnitude to the angular resolution Appendix B will point out the limits of reliability of the experimentally determined differential cross section as a measure of the true microscopic cross section. This will include a discussion of convoluting the microscopic cross section into the apparatus geometry to observe possible distortion resulting in its measurement.

Following a discussion of the possible uncertainties in the measurement (Chapter IV) of the total and differential cross sections, the data will be presented in Chapter V. Finally in Chapter VI, comparison of the data with theoretical calculations will be made. This will include a brief discussion of the various theories. It is the objective of this work to ascertain the limits of reliability of the theoretical approximations and to point out possible weaknesses from a comparison with the experimental data.

CHAPTER II

APPARATUS

Introduction

In its most simplified description the apparatus used for the present measurements of differential and total cross sections consisted of (1) a projectile source, (2) a collision region, and (3) a detection system. For this experiment (1) can be broken down into three parts: (a) ion source, (b) accelerator, and (c) charge exchange (neutralizer) cell. The detection system also consisted of numerous components including a metastable detector, scattered current and particle detectors, and a primary beam detector. In addition, components for provisions of beam focusing, collimation, beam steering, energy analysis, and data acquisition must also be included. The following is a description of each component, primarily in the order in which each device is encountered by the projectile.

Accelerator

Fast hydrogen atoms were produced in essentially a two-step process. First, a beam of protons was provided by an ion source and 1-30 keV accelerator, followed by focusing, mass selection, and refocusing. Secondly, the hydrogen ions were neutralized by charge transfer in a gas cell forming 1-30 keV hydrogen atoms.

The source of hydrogen ions was a commercially made Ortek Model 320 radio-frequency ion source consisting of a Pyrex bottle

with provisions for gas inlet, aluminum tip and sapphire sleeve, a radio-frequency oscillator, and a magnet providing an axial field. An extraction voltage of 0-5 kV across the bottle provided the initial acceleration. For low energy beams (1-5 keV) additional acceleration was provided by a Fluke 408B regulated power supply, while at higher energies (6-20 keV) a Soransen 5030-4 was utilized. It was found that for maximum ion output a combination of extraction voltage and acceleration beyond the source was required even in the low energy range. The source and its power supplies were maintained at high potentials, requiring insulation from the rest of the apparatus. Also the source was shielded to prevent radio frequency pick-up in the recording electronics.

Immediately upon exiting the source bottle the ions were focused by an Ortek 365D Einzel lens. Separation of H^+ ions from other ions (H_2^+ and H_3^+) was made by magnetic deflection. Current to the magnet was supplied by a Hewlett Packard 6296A regulated current supply. The proton beam was deflected 60° from its initial direction into a large cylinder housing the rest of the components of the apparatus. Between the magnet and the main chamber was another electrostatic focusing Einzel lens.

The source parameters (pressure, source magnetic field, and focusing) were adjusted for maximum beam output and stability. A pair of plates located between the first focusing element and the magnet was provided for horizontal deflection to compensate for any misalignment between the accelerator and the main chamber. The entire accelerator system was evacuated to a pressure of $5 \cdot 10^{-7}$ Torr by an

800 ℓ/sec CVC oil diffusion pump, with water cooled optical baffling, backed by a mechanical pump. Liquid nitrogen trapped hydrogen gas was leaked into the source via an Edward's needle valve. Although the source pressure was not measured directly, the base pressure in the accelerator, under typical operating conditions, rose to $\sim 2 \cdot 10^{-6}$ Torr.

Main Chamber and Modular Support

After refocusing, the ion beam entered a large cylindrical vacuum chamber 102 cm in diameter and 46 cm high. The chamber, constructed of type 304 stainless steel, was evacuated by two 6", 2440 ℓ/sec NRC oil diffusion pumps, backed via a common roughing line by a Welch 1397B mechanical pump. Sorbent traps were provided between the diffusion pumps and the main chamber to inhibit backstreaming of oil into the system. Pressures as low at $1 \cdot 10^{-7}$ Torr were achieved.

All electrical, pumping, and gas inlet connections were made through ports in the bottom plate. Three multipinned and several single pinned feed throughs provided voltage to and signals from the components inside the main chamber. Two diametrically opposed ports were located on the cylinder of the main chamber. One port fitted with an isolation valve was the inlet for the primary ionic beam leaving the accelerator. The other port, fitted with a glass window, was used solely for observational purposes.

Components inside the chamber (see schematic view in Figure 1) were placed on rails which were supported from a massive, hollow central hub. One end of one of the rails was secured directly to the hub while the other end was attached to the hub by a rigid rod. The

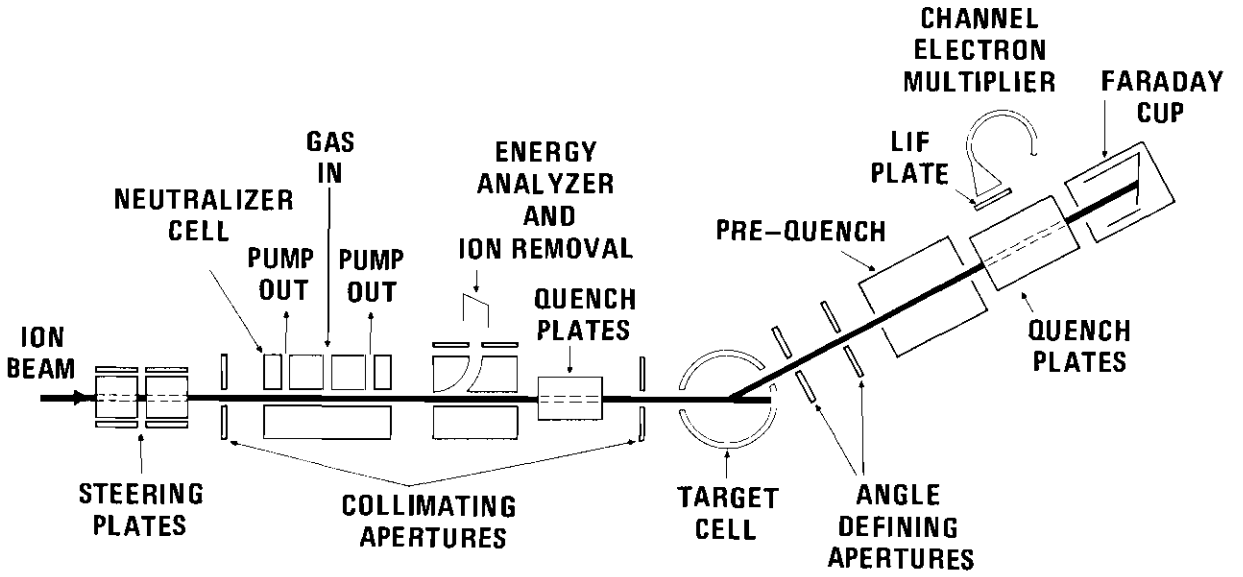

Figure 1. Schematic of Components in Main Chamber.

other rail rested on a flat plate firmly attached to the hub, thus allowing this rail to be mobile. The hub end of the rail was attached to a ball bearing race which gave it the freedom to rotate about the hub. The other end rested on a single captive steel ball. The movable rail could then swing through a wide range of angles with respect to the stationary rail, so that components on the rail could detect scattered flux. Movement of the rail was performed externally by a rotary motion vacuum feed through. In addition, continuous scanning of a range of angles was permitted through the use of a high torque motor drive.

Except for the target cell all the components rested on the fixed and movable rails. Both rails were long flat plates, with two square ridges running the lengths of the plates. An individual component was secured to a support stand which rested on the two ridges. A screw through one side of the support was tightened against one of the ridges; hence positioning of the components was well determined. Also, alignment of the components with respect to each other was assured even when individual components were removed from and replaced to the rail.

Each component stand was equipped with horizontal and vertical slides. The component was then attached to a flat plate which fitted into the slides. After proper positioning, the plate was then tightly secured to the support stand by set-screws.

Beam Positioner

Upon entering the main chamber final positioning of the beam was required for proper injection into the collision region. An

electrostatic positioner consisting of four pairs of plates provided horizontal and vertical deflection of the ion beam prior to neutralization. Voltage to all the plates was provided by a well regulated Fluke 1402B power supply.

Beam Collimator

Collimation of the incoming beam was provided by two rectangular holes in stainless steel plates. The two slits were 34 cm apart, with the second slit 7.4 cm from the center of the collision region.

Two sets of collimators were used during the experiment (refer to Figure 2). The larger set (both of which were 0.1 $\pm$ 0.005 cm wide) was utilized for scattering data in the 0.5°-2.0° range. A smaller set of apertures (0.037 $\pm$ 0.005 cm wide and 0.1 $\pm$ 0.005 cm high for the slit nearest the target cell; and 0.047 $\pm$ .002 cm wide and 0.1 $\pm$ 0.005 cm high for the farthest slit) were required so that detection at smaller scattering angles (below 0.5°) could be achieved without interference with the primary projectile beam. These apertures were also used for large angles (>2.0°) when single-particle detectors (channeltrons) were employed to measure scattered flux.

Neutralization Cell

Fast hydrogen atoms were formed by the process of charge exchange neutralization of a fast proton beam. For this purpose a gas target housed in a cell, the center of which was located 35 cm from the center of the primary collision cell, was supplied to create neutrals by the process

$$H^+ + X \rightarrow H^o + X^+ \quad . \tag{4}$$

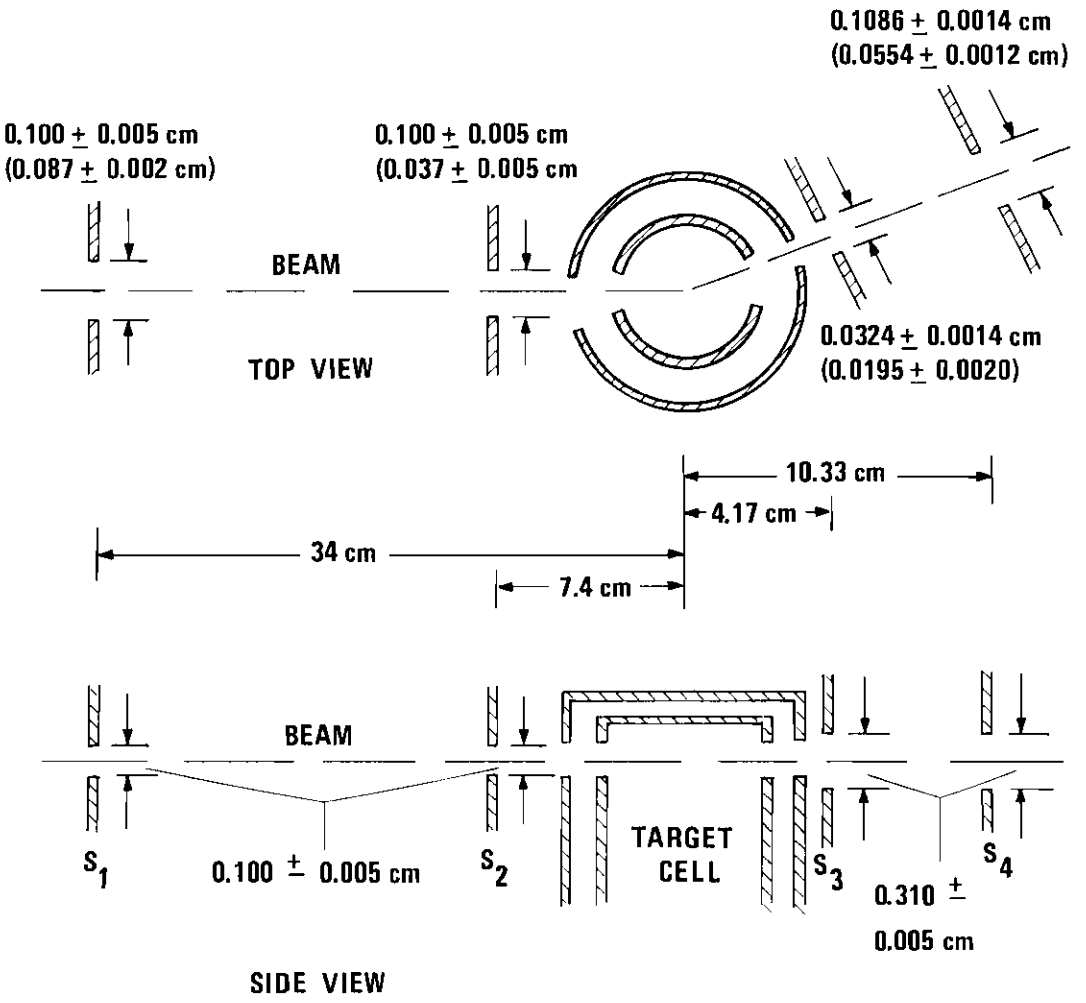

Figure 2. Top and Side View of Collimating Apertures with Dimensions. (Note: Dimensions in Parentheses Correspond to Alternate Set of Apertures Incorporated into the Experiment.

The cell was formed from two stainless steel plates (see Figure 3), with the bottom plate containing a rectangular groove 0.25 cm square running the length of the plate. The top plate had two holes at either end which were interconnected by a steel bellows and led via a manifold to a pumpout station. A central hole in the top plate provided a gas inlet for the cell.

The pumpout connection at the ends of the cell were required to minimize leakage of neutralizer gas into the large vacuum chamber, and hence, restricting a rise in base pressure.

The neutralizer cell manifold had three ports leading to an ion gauge, capacitance manometer, and pumping system. The pumping system consisted of a 100 ℓ/sec oil diffusion pump backed by a Welch 1402B mechanical pump. The diffusion pump was equipped with a water cooled baffle, a liquid nitrogen cooled trap, and an isolation valve.

Neutralizer gas was provided from a commercially purchased high purity cylinder, and cold trapped for condensable impurities. The gas was throttled by an Edward's needle valve, before entering the cell through the central gas inlet hole. The pressure inside the cell was not measured directly, since direct knowledge of the pressure was not necessary for the present experiment. However, the pressure at the entrance and exit of the cell (as measured by the ion gauge located at the manifold) was normally $\sim 5 \cdot 10^{-4}$ Torr. In general, the neutralizer gas was the same as the target gas. The gas pressure was high enough to produce maximum neutralization while limitations were placed on the rise in the base pressure ($1 \cdot 10^{-6}$ Torr) of the main chamber.

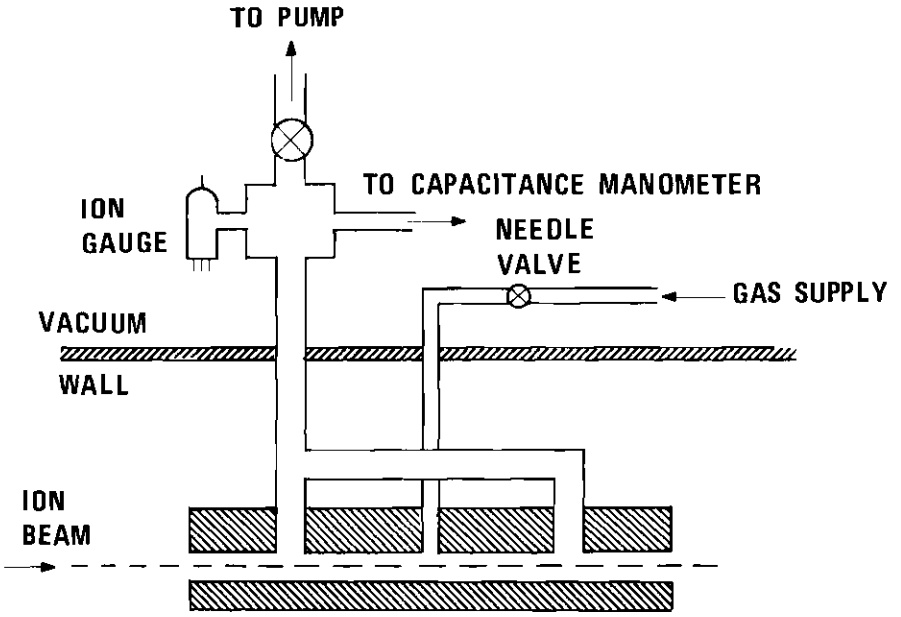

Figure 3. Schematic of Neutralizer Cell.

Electrostatic Analyzer

Located between the neutralization cell and the second collimator was an electrostatic analyzer, primarily used for precise determination of the beam energy. This component consisted of two cylindrically shaped plates which, when the proper voltage was applied, deflected the ion beam 90° with respect to the incoming trajectory. The deflected ion current was then measured by a plate at the top of the analyzer. By knowing the curvature of the plates the voltage applied across them determined the velocity (hence the energy) of the beam.

Two power supplies were used so that the two plates could be biased separately; the bottom plate was biased negatively with respect to ground, while the top plate was biased positively. The power supplies (Fluke model 1405) were calibrated and found to be accurate to within 0.1%. The energy resolution was determined by varying the power supply voltage and observing the current intensity; the full width at half maximum indicated a resolution of $\pm$2.0%.

Target Cell

A gaseous target for the collision was housed in a cell which rested on top of the central hub. The cell was specially designed to allow for rotation without obstruction of the incoming projectile beam.

The cell consisted of two concentric cylinders (see Figure 4). The inner cylinder which was 5.08 cm in diameter was fixed in place to the hub. The entrance was a 0.635 cm hole, while the exit was a narrow slot 0.32 cm high and ~2.6 cm in length. Thus particles

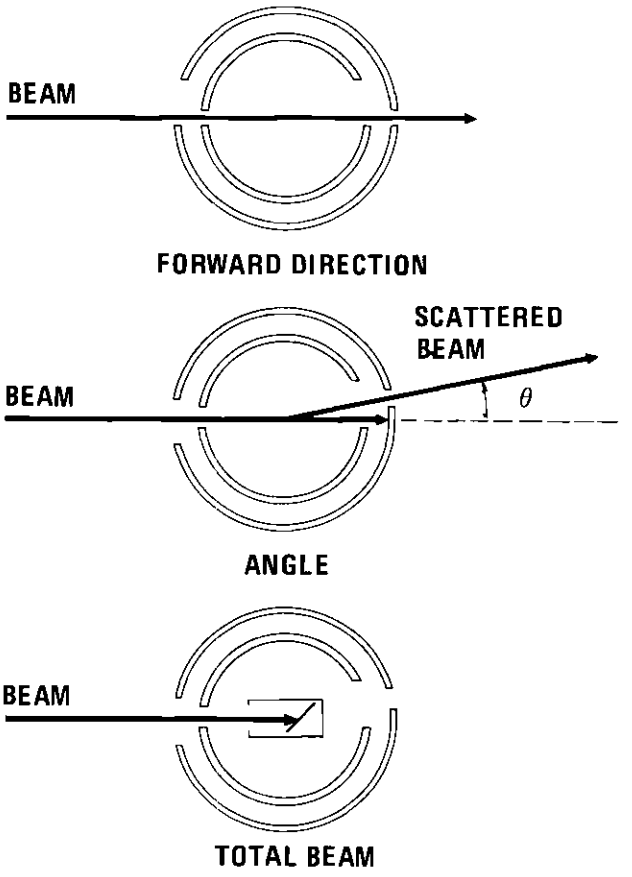

Figure 4. Detailed View of Target Cell: Upper Diagram Shows the Target Cell Set to $\theta_c = 0$; Middle Shows the Target Cell Set to Some Scattering Angle; Lower Diagram Shows Projectile Flux Detector in the Target Cell.

within the cell could emerge from a wide range of scattering angles (-7.0° to $+45.0^\circ$). The outer cylinder (8.26 cm high by 6.03 cm in diameter) rested on top of the hub, but was free to rotate about the inner cylinder. A narrow slot 0.32 cm high and 2.65 cm wide provided the entrance for the incoming beam, and on the other side a small hole 0.635 cm in diameter allowed scattered particles to exit the cell. The first of two angle-defining apertures (see page 17) was placed against this exit hole. The entrance apertures of both the inner and outer cylinders were large enough to allow the full projectile beam to enter the cell. The two cylinders were electrically insulated from each other and from the rest of the apparatus by strips of mylar so that ions (or electrons) striking either cylinder could be measured; also biasing voltages could be applied.

Target gas was supplied to the cell from below through the hollow hub. The gas originated from a commercially purchased high purity, high pressure gas cylinder and was introduced by a slow leak through an Edward's needle valve. Between the needle valve and gas cell was an electrically operated pneumatic valve which could be used to temporarily cut off gas flow to the cell without altering the setting of the leak valve; this was used in assessing background signals due to scattering from residual gases in the cell. While the automatic valve was closed another electrically operated valve was opened to a pumping system consisting of 80 ℓ/sec CVC oil diffusion pump with a water cooled optical baffle and sorbent trap, and backed by a mechanical pump, maintaining a good vacuum ($<1.10^{-5}$ Torr) along the gas feed line. To further insure purity of the gas, the target gas feed line (as well as the neutralizer

gas feed line) passed through a cold trap containing either a frozen CO_2 and acetone mixture or liquid nitrogen, depending on the nature of the gas used.

The pressure of the target gas was measured directly by an MKS capacitance manometer which was referenced to the pressure in the main chamber. The double cylinder arrangement of the target cell reduced the leakage rate of gas into the main chamber so that the difference in pressure inside and outside the cell was at least two orders of magnitude. A set of three electro-pneumatic valves was provided between the capacitance manometer and either the target cell, neutralizer cell, or the main chamber. The two valves to the target and neutralizer cells allowed for a pressure measurement in either. The valve to the main chamber allowed the two sides of the Baratron to be connected to the main chamber and so permitted the zero of the device to be checked while target gas was present in the cell.

Scattered Flux Collimator

Positioned against the exit hole of the outer cylinder of the target cell was the first of two collimating apertures which define the angle of scattering of the post collision ions and atoms. The two slits were mounted at opposite ends of a cylinder which was secured to a support resting on the movable rail. Each slit was formed by placing two thin sheets of stainless steel against two pins located above and below a larger hole which then became partially masked. These pins were parts of slugs which could be removed and replaced by pins of different diameters. This method was feasible for pins with diameter greater than 0.03 cm; however, for smaller slit widths it was impractical to machine

smaller pins. For smaller slits, a specially cut piece of thin stainless steel was placed against the pins, with a portion of the steel sheet projecting toward the center of the hole, thereby creating a smaller aperture.

During the progress of the experiment two sets of collimators were used (see Figure 2). For data taken in the 0.5°-2.0° range slit sizes of 0.0324 $\pm$ 0.002 cm and 0.1087 $\pm$ 0.002 cm width were used. Both slits were 0.31 $\pm$ 0.005 cm in height with the smaller of the two slits located 4.17 $\pm$ 0.01 cm from the center of the collision cell, while the larger slit was 14.33 $\pm$ 0.02 from the center. For the small angle (<0.5°) data and subsequently the single particle counted large angle data, the slit sizes were changed to 0.0195 $\pm$ 0.003 cm and 0.0554 $\pm$ 0.003 cm widths; all other dimensions remaining the same. A discussion of the angular resolution defined by this slit arrangement will be discussed in Appendix B.

Metastable Hydrogen Detector

Next, along the scattered beam path on the movable rail was the detection system for measuring metastable hydrogen atoms. The principle upon which detection of H(2s) atoms was based was the Stark effect. An electric field perturbing the states of hydrogen 'mix' the long-lived $2s_{1/2}$ state with the short-lived $2p_{1/2}$ and $2p_{3/2}$ states, thereby reducing the effective lifetime of the $2s_{1/2}$ state.

The detection system (see Figure 5) consisted of a pair of electrostatic plates (termed 'quench' plates), a cylindrical electrode in front of the quench plates (called 'pre-quench'), and a funneled electron multiplier above the quench plates.

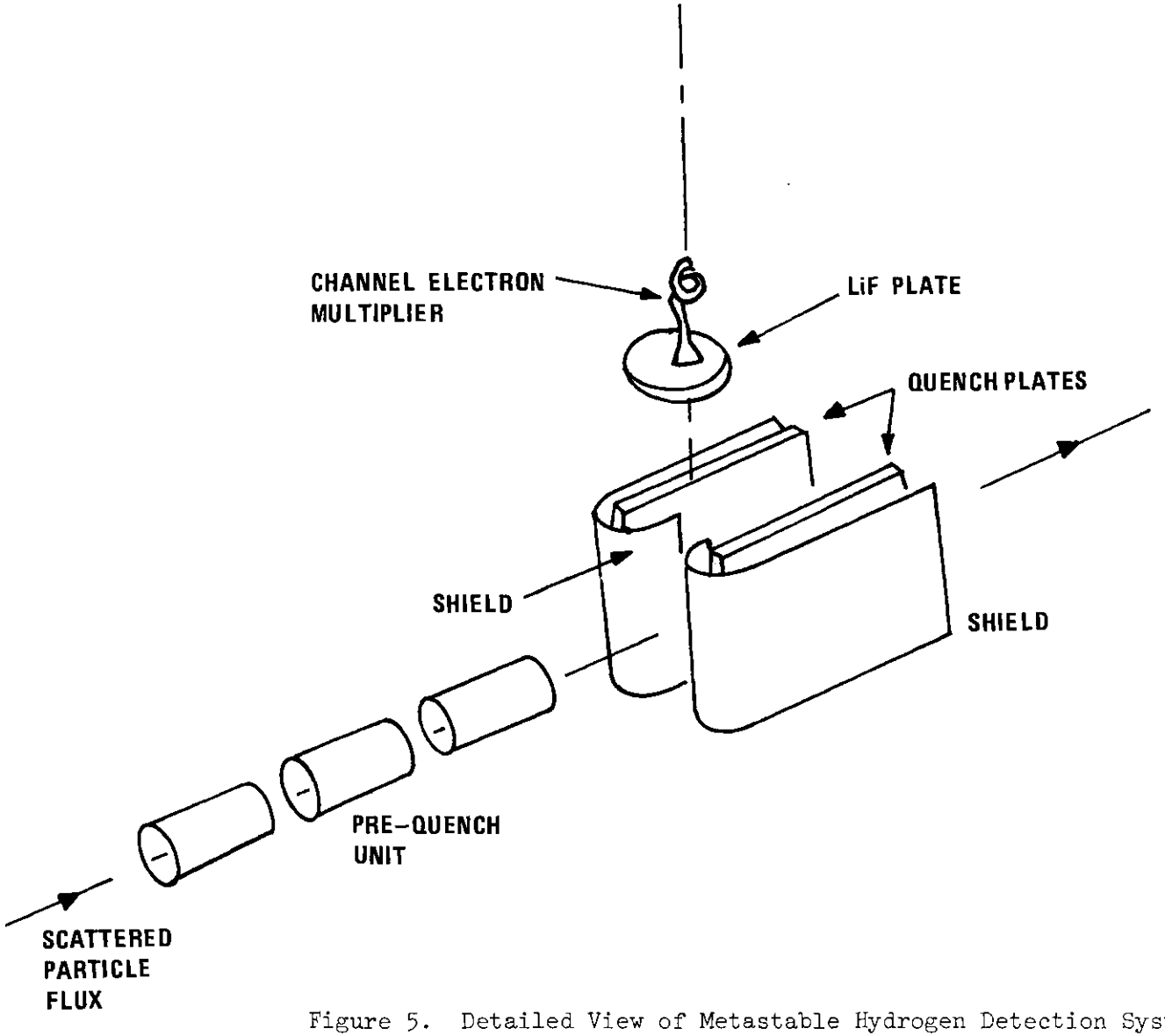

Figure 5. Detailed View of Metastable Hydrogen Detection System.

Stainless steel quench plates 2.54 cm apart, 7.6 cm in length, and 3.2 cm high were used to provide a transverse electric field. To eliminate quenching outside the viewing region of the electron multiplier, a grounded shield was placed around the front end of the quench plates and projecting 2.0 cm into the quench region. The voltage applied across the plates ranged from 400 V - 800 V depending on the beam energy.

Detecting photons emitted in the quench region was a Bendix 4039 channel electron multiplier with a LiF window. The combination limited the wavelengths accepted to 1100-2000 Å so that the only atomic hydrogen emission falling in this range is the Lyman-alpha 1216 Å photon from the H(2s) atom. In addition, grounded grids were placed on either side of the LiF window; the above grid made a uniform cutoff of the high electric field in the electron multiplier at the mouth of the funnel while the grid below the window inhibited charged particle build-up on the window itself. The channeltron was always operated in a saturated mode (operating voltage of 3000 V) and in a pulse counting mode.

The pre-quench unit which was cylindrical provided an axial field for quenching metastables prior to the detection region, while at the same time leaving the trajectory of ions in the scattered beam undisturbed. The inclusion of the pre-quench unit was necessitated by the fact that a strong electric field applied in the quench region slightly altered the background signal. (This was most likely due to accelerating ions or electrons into the quench plates, resulting in ultra-violet emission.) By removing metastables prior to detection

this background could be easily assessed in the analysis of the H(2s) data (see Chapter III).

Ion-Atom Current Detector

Measurement of ions or atoms in the scattered flux for scattering angles below 2.0° was made by a device which had the combined features of a Faraday cup and a secondary electron detector (Figure 6). The detector was located on a component stand situated at the end of the movable rail.

The base of the detector consisted of three plates inclined at an angle of 30° with respect to the beam direction. The central and right plates were electrically joined, with the common lead going to a single pinned vacuum feed-through. The lead from the left plate was brought to a separate feed-through. A plate above the inclined back plates was used for collection of secondary electrons. The inside surface of the detector insulated from the above and back plates was electrically biased to suppress the escape of secondary electrons from the detector.

In its operation as a Faraday cup the left back plate and top plate were connected to the right and central plate (see Figure 6) by an external switch and coaxial relay. Charged particles in the scattered beam could be measured directly with no loss of electrons ejected from the rear plates in the manner of a conventional Faraday cup. For detection of neutrals the top and left plates were disconnected from the other rear plates. H^+ ions could be deflected onto the left plate by an electric field applied on the quench plates in the metastable atom detector. The current measured due to the loss

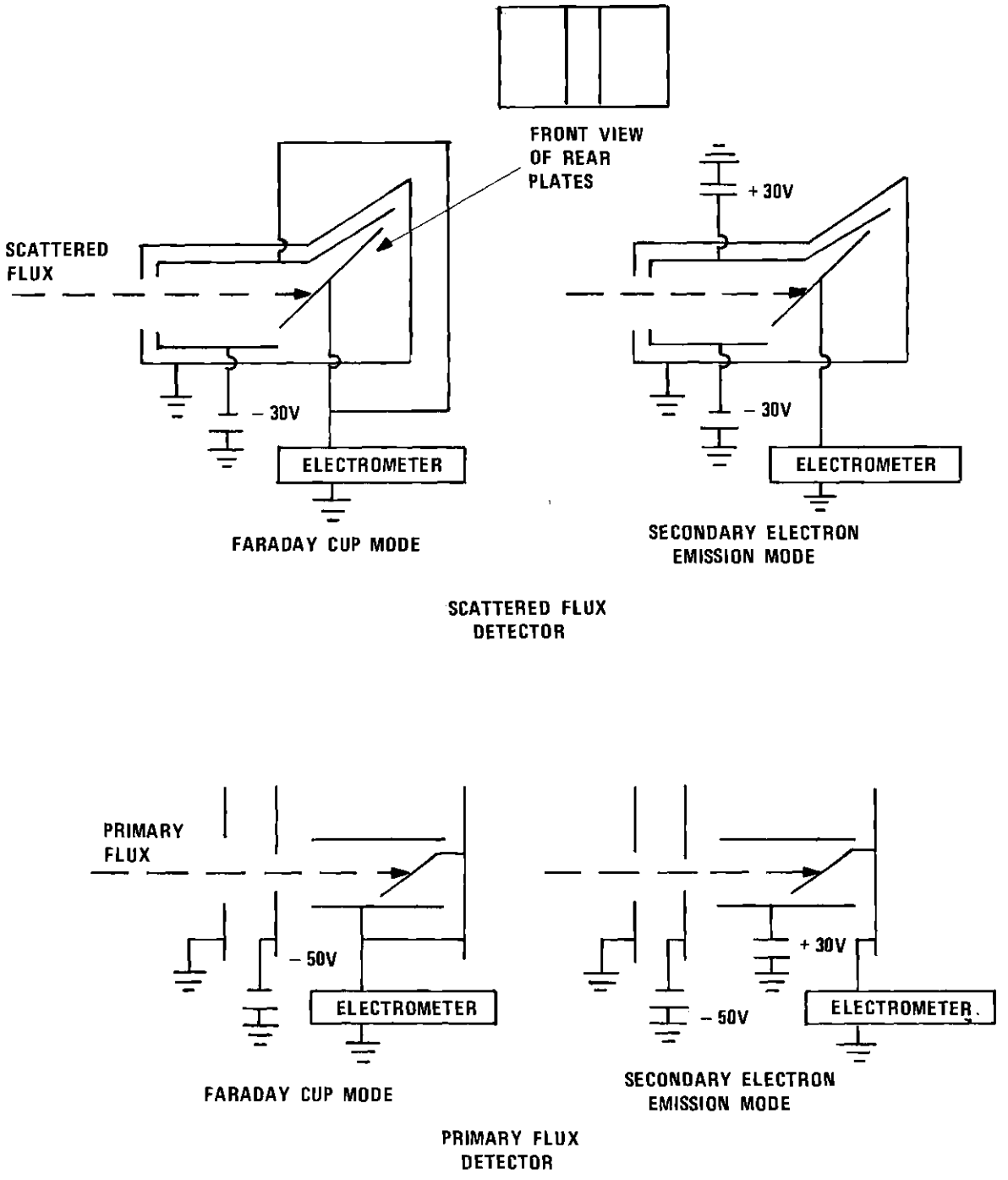

Figure 6. A. Schematic of Scattered Flux Detector.
B. Schematic of Primary Flux Detector.

of secondary electrons from the center plate was directly related to the flux of neutral hydrogen atoms striking the back plate. The method of analysis in determining the absolute hydrogen flux (hence the absolute cross section) is described in Chapter III.

The very low scattered current signals (10^{-9} - 10^{-15} amps) detected during the course of the experiment were measured by a vibrating reed electrometer (Cary model 31). The pre-amp unit was equipped with three precision resistors (10^{10}, 10^{11}, and 10^{12} Ω) providing current measuring ranges down to 10^{-15} amp. The output of the electrometer was calibrated against a low current source made by Gyra Electronics. The calibration was performed over overlapping scales and resistor settings to provide a consistent set of correction factors so that the resulting measurement was considered to be accurate to within 1.0%. When a Faraday cup arrangement was used to measure the unscattered primary projectile flux the current measurements were made by a Keithley 410 micro-microammeter calibrated in the same manner as the Cary electrometer.

Ion-Atom Particle Detector

For the large angle (>2.0°) scattering data in which fluxes were too small for current detection, another detector was utilized in place of the current detector described in the previous section. The detector was composed of two channel electron multiplier tubes (similar to the channeltron in the metastable hydrogen detector) and a conventional Faraday cup; all were mounted side-by-side on a standard component stand. One of the multipliers was placed in the center with the other channeltron and Faraday cup on either side. Charged

particles were deflected electrostatically (by the quench plates) into the left channeltron, while undeflected neutrals were detected by the central channeltron. The inclusion of the Faraday cup in the detector was necessitated by the initial set-up procedure in which the primary ion current must be measured (for determination of intensity, symmetry, etc.). These currents were much too large ($>10^{-9}$ amp, i.e., $>10^{+10}$ counts/sec) for the channeltron and would have in fact damaged it.

The channeltrons were wide funneled Bendix type 4039, with an entrance large enough to collect all particles emerging from the scattered slit collimators. Both were powered by a Fluke power supply and operated in a saturated counting mode. A grounded grid with 99% transmission was placed in front of the funnels. Count rates were held to under 1000 counts/sec to insure single pulse counting.

Primary Beam Detector

The incoming neutral flux intensity was determined by a combination Faraday cup-secondary electron detector located in the target cell region (Figure 4). Mounted on a long rod attached to a linear drive vacuum feed-through the detector could be driven vertically into the beam path from below. The linear motion feed-through was mounted to the bottom plate of the central hub.

The detector (Figure 6) was composed of a single inclined plate inside a cylinder. In front of the cylinder were two steel plates, the front end of which supported the assembly. The second plate had a 0.64 cm hole and was biased negatively with respect to the grounded front plate to repel electron escaping from within the detector. The cylinder was either connected (external to the vacuum system) to the

back plate for use as a Faraday cup; or was biased positively for collection of secondary electrons when used for neutral detection. The method for determining the neutral projectile flux is described in Chapter III.

Again, secondary electron currents resulting from neutral hydrogen impact on the detector plate was measured by the Keithley 410 micro-microammeter.

Data Acquisition

In general all signals resulting from the scattered particle detectors (metastable detector, H^+ and H^o detectors) were converted to digital form and logged on Ortek Mode 430 scalers; these numbers were periodically printed out on a Teletype (see Figure 7).

Signals from the channeltron, in both the metastable detector and the particle detectors (when used), were in pulse form. These were simply amplified, shaped, and sent through a discriminator to remove low level electronics noise; finally, they were fed into scalers.

Scattered currents were recorded by sending the voltage output of the electrometer into a voltage-to-frequency converter; the resulting pulse rate proportional to the scattered current intensity was fed into a scaler and subsequently printed out.

Normally, the scattered current data was acquired simultaneous to the channeltron data; the ratio of the two signals was quite reliable since it was independent of minor fluctuations of beam intensity, pressure, etc. Signals from the metastable detector were often quite small (<1 $^{count}/_{sec}$) and required counting times of 100-800 seconds

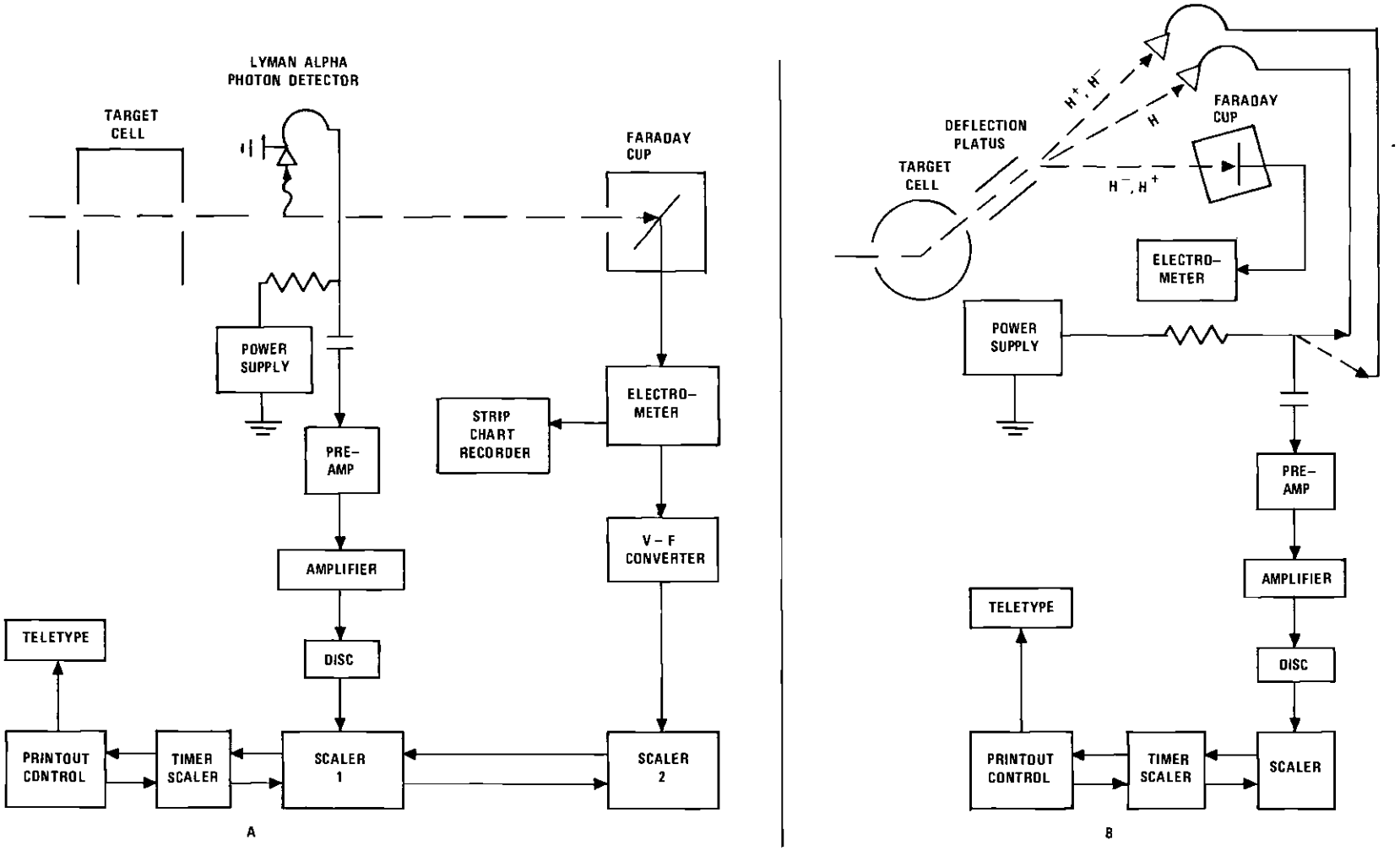

Figure 7. Block Diagram of Data Acquisition System. A. System Used for Measurements Made at Angles $\theta_c < 1.5^o$; B. System Used for Measurements Made at Angles $\theta_c > 1.5^o$.

to achieve statistical accuracy. The additional information such as beam intensity, target pressure, and electrometer scale settings were recorded manually.

CHAPTER III

EXPERIMENTAL METHOD

Introduction

The manner in which the differential cross sections for formation of H^o, H^+, and H(2s), and the total cross section for formation of H(2s) were obtained is described in this chapter. The discussion includes a description of the method for determining the projectile and scattered flux intensities, the target density, and the scattering angle.

Beam Profile

In preparation for scattering measurements an ion beam is directed to the Faraday cup through two collimating apertures and two angle defining apertures. This becomes the path followed by forward scattered hydrogen atoms exiting the charge transfer cell. Two items of primary importance to be determined are that (1) the projectiles move along trajectories parallel to the normal of the planes of the collimating apertures; and (2) the scattering angle, $\theta_c = 0$ is accurately known. Information for (1) and (2) are found from the beam profile, which is a measure of the projectile flux transmitted through all the apertures as a function of angle.

The scanning procedure was performed by a continous rotation of the Faraday cup and angle collimators about the target cell center and monitoring of the detector current by feeding the output of the

micro-microammeter into a strip chart recorder. A rule with scribe marks in 10 minutes of arc intervals located on the moving platform of the detection system, and a fixed pointer was visible through the viewing port in the main chamber. Aided by a telescope, observation of the scribe marks passing the pointer was recorded by manually sending a pulse into the strip chart recorder, thus providing indications of the angle in 10' intervals along the beam profile.

If the center of the projectile flux is moving along a line which is not parallel to the center line of the slit system the resulting beam is asymmetric. This beam scan symmetry is required prior to any data run; and scans were made periodically during and after the data run to determine the acceptability of the data. An additional requirement is that the projectiles move along parallel trajectories. There are essentially two sources of divergence of the incoming beam: (a) a divergence of the ion beam entering the charge exchange cell and (b) divergence of the hydrogen atoms exiting the cell due to scattering. It was not possible to directly assess the percentage of divergent ions in the beam and the extent of divergence; however, the dimensions of the two collimating apertures placed an upper bound of 0.05° divergence. Although at each energy a different set of focusing and deflection voltages was required the widths of the beam scans remained unaltered, indicating that beam output optimization conditions resulted in a nearly parallel beam of projectiles.

With the Faraday cup operating in the secondary electron emission mode scans of the hydrogen atom beam flux were made. A broadening of the hydrogen atom profile as compared to the H^+ profile

was considered to be due to scattering. From this comparison a divergence of 0.045° was observed.

The determination of the point on the rule for which $\theta_c = 0$ was made by two independent methods. The first method was by determining the center line of the beam scan. (Since the beam scans were symmetric, this could be done quite accurately.) The second, more direct method was by measuring the angular distribution of scattered particles (when a target gas is present) at large angles on both sides of $\theta_c = 0$ and taking the line of symmetry. The two methods agreed with each other to within 0.02°. Normally the second method was less practical since it required a duplication of data; and, in general, the first method was used.

Neutral Beam Set-Up

With a hydrogen ion beam properly aligned and collimated, gas was admitted into the neutralizer cell. At projectile energies of 5 keV and higher helium was chosen as the neutralizer gas, while argon was used at lower energies due to its greater charge transfer cross section. In the initial collision three processes can occur

$$H^+ + X \rightarrow H^+ + X \tag{5}$$

$$H^+ + X \rightarrow H^o + X^+ \tag{6}$$

and

$$H^+ + X \rightarrow H^- + X^{++} \tag{7}$$

where X is helium or argon. In subsequent collision we can also have

$$H^o + X \rightarrow H^o + X \tag{8}$$

$$H^{o} + X \rightarrow H^{+} + e + X \tag{9}$$

$$H^{o} + X \rightarrow H^{-} + X^{+} \tag{10}$$

and

$$H^{-} + X \rightarrow H^{-} + X \tag{11}$$

$$H^{-} + X \rightarrow H + e + X \tag{12}$$

$$H^{-} + X \rightarrow H^{+} + 2e + X \quad . \tag{13}$$

The cross sections for (7) and (13) are small and are not considered to be important in the growth rate of H^{o}.[22] Reactions (5), (8), and (11) are elastic scattering and do not contribute to the growth and depletion of atoms and ions formed in the collisions cell. The neutralizer cell was operated at high pressures to achieve maximum neutralization, so long as the main chamber base pressure was not raised above $1.5 \cdot 10^{-6}$ Torr. (This pressure was arbitrarily chosen as the limiting pressure for which it was certain that scattering off of background gas remained a negligible effect.)

The flux exiting the cell consisted of hydrogen atoms in the ground and excited states, H^{+} and H^{-} ions. The ions were removed electrostatically by the electrostatic analyzer. The high field (500 $^{V}/cm$) also Stark mixed the $2s_{1/2}$ states with $2p_{1/2}$ and $2p_{3/2}$ states inducing decay to the ground state. It was found, by applying a quench field in the detection region and observing the net signal, that no measurable amount of H(2s) atoms remained in the neutral flux.

The 2p states also decay long before the hydrogen projectile reaches the collision cell.

As the quantum number n for an excited hydrogen atom increases so does the lifetime.[23] The distance between the neutralizer and target cell is sufficiently long so that excited hydrogen in principal quantum states less than five can de-excite to the ground state; however, more highly excited states can persist in the beam flux.

Thus for sufficiently high n for which the lifetime is comparable to the transit time of the hydrogen atom from neutralizer to collision cell, it is necessary to assess the influence of highly excited hydrogen on the scattering data. To this end efforts were made to alter the excited state content of the hydrogen flux emerging from the neutralizer cell by variation of neutralizer gas and gas pressure; helium and argon were interchanged as neutralizers, while operating pressures for both gases were not influenced by any of these tests, indicating to the author that highly excited states in the neutral beam flux did not affect the data.

Beam Monitor

There was no provision for directly monitoring the projectile beam intensity while measurements of scattered flux were being made. However, an indirect monitor of the stability of the beam intensity was made possible by deflecting the ion beam exiting the neutralizer cell into the Faraday cup of the electrostatic analyzer. Variation in ion intensity implies a corresponding variation in neutral flux intensity, invalidating the data run. A $\pm$3% change in intensity was considered an acceptable level of stability.

Below 5 keV, this method of monitoring the beam was not feasible since the voltage required to deflect the ion beam into Faraday cup was insufficient for quenching metastables in the neutral flux. For that data, periodic checks of the beam intensity was made directly by rotating the scattered flux Faraday cup back to the $\theta_c = 0$ position. The same criterion for beam stability was followed.

Target Density

The density of the target gas was determined from the pressure in the gas cell by the perfect gas law yielding the relationship

$$N_T = 3.24 \cdot 10^{13} P \tag{14}$$

where P is the pressure in microns. (1 Micron = 10^{-3} Torr.)

The pressure in the target cell was measured directly by the capacitance manometer which had previously been calibrated against a trapped McCleod gauge and found to be accurate to within 5.0%. Due to a difference in temperature between the manometer sensor and the gas cell, a thermal transpiration[24] correction was made.

When the manometer was operated on either its 0.1 micron or 1.0 micron range, a zero drift in the electronics by as much as $\pm$5.0% in a period of 1-2 minutes was observed. Since it was necessary to make accurate measurements of the pressure while gas was present in the cell, a set of electro-pneumatic values was used to switch the pressure sensor from the target cell to the main chamber (against which the sensor was referenced). Repeated measurements of the pressure was then made by alternating the sensor from target cell to main chamber and subtracting the two readings.

Single Collision Conditions

The gas density was held low enough to prohibit multiple collisions. The acceptable pressure range was determined by plotting the signal of the scattered particle flux against pressure and noting the region of linearity. In general a plot was made at each energy both for scattering angle, $\theta_c = 0°$ and $\theta_c = 1°$. For a He target the maximum acceptable pressure was 1.5 microns while for Ar the maximum pressure was 0.5 microns.

Pressure Profile

From the dimensions of the gas cell and the distance from the gas inlet to the projectile path, the gas density was considered to be uniform throughout the collision path within the cell. The pressure outside the cell was essentially zero (i.e., a pressure differential greater than 100 exists between the cell and the main chamber). In the determination of the variation in pressure near the entrance and exit holes for a cell of this type the pressure reduces to a negligible amount at a distance away from the hole equal to the diameter of the hole.[25]

The collision path length is determined by the geometry of the angle defining slits (see Appendix B). For most of the angles at which data was taken this path length lay completely within the cell, where the density is constant. However, near 0.5° for the large set of collimating apertures and 0.2° for the small set the path length extended beyond the cell in which case the effective cell length was used. From the discussion of the pressure profile for the cell, the length was taken to be the diameter of the inner cylinder, 2.5 cm

plus the effective diameters of the entrance and exit holes 0.2 cm and 0.2 cm respectively.

Detection of Projectile H^o

The projectile flux, N_B (particles/sec), was determined by measuring the current of secondary electrons I_B (amp) ejected from the back plate of the target cell Faraday cup due to H atom impact. Thus

$$N_B = \frac{I_B}{\gamma^o e} \tag{15}$$

where γ^o is the coefficient for secondary electron emission and e is the charge of an electron. Since it has been found[26,27,28] that for a given impact energy the ratio γ^o/γ^+ (where γ^+ is the coefficient for H^+ impact) is independent of the metalic surface, the value of γ^o was determined by a direct measurement of γ^+ and the known value of γ^o/γ^+ at each impact energy.[29] Figure 8 shows a plot of γ^o/γ^+ versus energy in the range, 1-20 keV. The secondary emission coefficient, γ^+, was found by setting up an H^+ beam and (1) operating the detector in the Faraday cup mode and measuring directly the H^+ ion current i^+; and (2) operating the detector as a secondary electron detector giving a current $i_T = i^+ + \gamma^+ i^+$.

Detection of Scattered H^o

The differential cross section for scattered H^o is given by

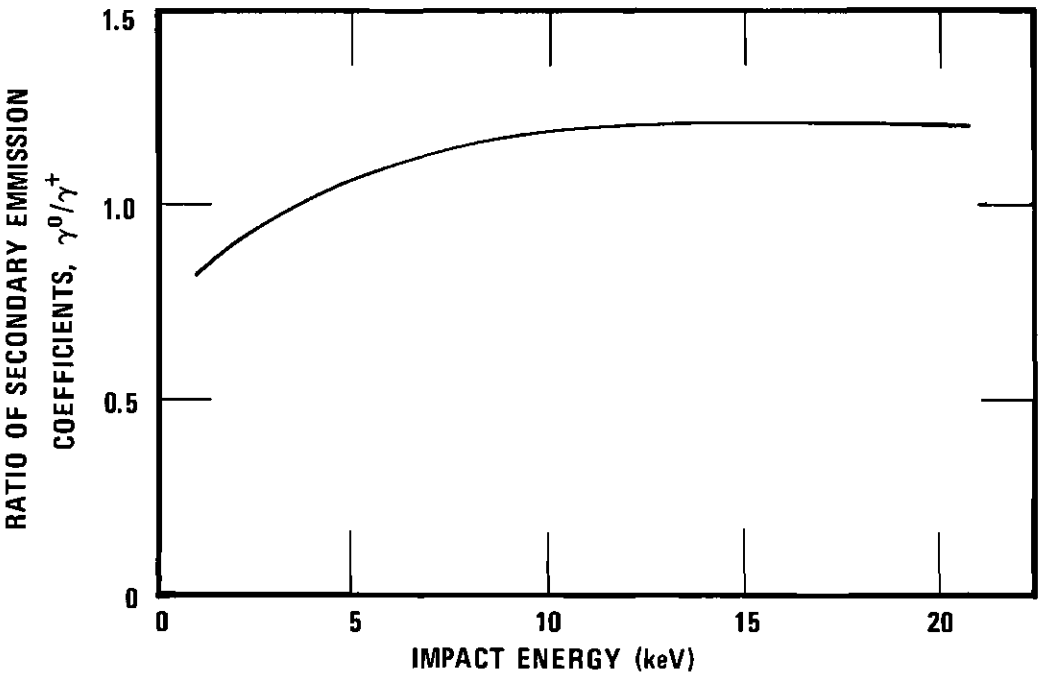

Figure 8. Ratio of Secondary Emission Coefficients, $\gamma^{\circ}/\gamma^{+}$ as a Function of Impact Energy.

$$I^{o}(\theta_c) = \frac{N_s^{o}}{N_B N_T G_{AVG}(\theta_c)} \tag{16}$$

where N_s^{o} is the flux (in particles/sec) of scattered H^{o}, N_T is the target density (in particles/cm^3), and $G_{AVG}(\theta)$ is the average value of the geometrical factor $\int\omega dx$ (see Appendix B for details of the averaging procedure). Data was taken in three angular regions: (1) 0.2°-0.5° where only relative angular distributions were measured with the small set of collimating apertures (see Chapter II for description and dimensions); (2) 0.5°-2.0° where the scattered flux was measured absolutely by the ion-atom current detector with the large collimating apertures; and 1.5°-6.0° where the flux was detected by the ion-atom particle detector.

An absolute measurement of the cross section was made, using Equation 16, at 1.0°. The data in the 1.5°-5.0° range was then normalized to the 0.5°-1.5° data, thus yielding absolute cross sections in the entire 0.5°-6.0° range. A discussion of the calibration procedure follows.

Absolute Calibration

As in the case of the primary neutral flux measurement the scattered flux N^{o} was found by operating the scattered flux detector in the secondary emission mode (Chapter II) yielding a current I^{o} related to N_s^{o} by Equation 15. Again an absolute measurement requires a knowledge of γ^{o}. Similar to the method employed for projectile beam detection, a determination of γ^{+} was made.*

*Since ions are also present, the quench field was utilized for deflection of ions away from the central plate of the detector at which the neutral flux is being measured.

The detector was set to some large angle (normally ~1.0°) and the following three currents were measured: i^+, i^o, and i_T where

$$i_T = i^+ + \gamma^+ i^+ + i^o \ , \tag{17}$$

i^+ is the current of scattered ions; $\gamma^+ i^+$ and i^o are the currents of secondary electrons due to ion and neutral impact respectively. Because of heavy bombardment of the detector plate for long periods of time, γ^+ was found to vary across the surface with a minimum appearing in the forward direction; however, at angles outside the main beam edge γ^+ was found to be constant.

Once γ^+ was determined, N_s^o could be found. Coupled with a measurement of N_B and N_T, an absolute determination from Equation 16 was made. The relative distribution was then normalized to the measurement at 1.0°.

The large angle (1.5°-5.0°) data divided by $G_{AVG}(\theta)$ appropriate to the dimensions of the small apertures (Chapter II) was then normalized to the 0.5°-1.5° data.

Effect of H^-

The charge transfer process

$$H + He \rightarrow H^- + He^+ \tag{18}$$

give rise to H^- in the scattered flux; an appreciable H^- current could therefore tend to an erroneous determination of γ^+ by contributing a negative current signal to the detector. An assessment of the H^- intensity was determined by operating the detector as a Faraday cup and measuring (1) the current of ions to the central-right detector

plates and (2) the current to the central-right detector plates with negative ions swept away from the central plate onto the left plate; no difference in signal could be detected. It was thus concluded that the H^- current (hence the cross section for Equation 18) was at least two orders of magnitude below H^+.

Detection of Scattered H^+

A direct measurement of the scattered H^+ ion current (by operating the detector as a Faraday cup) was made to obtain the angular distribution for Equation 3 in the 0.5°-2.0° range. For the 2.0°-5.0° range positive ions were swept (via the quench field) onto the left channeltron of the scattered flux particle detector. At each energy an absolute measurement was made at 1.0° by the equation

$$I^+(\theta_c) = \frac{N^+}{N_B N_T G_{AVG}(\theta_c)} \tag{19}$$

where N_s^+ is the ion current I^+ divided by the charge of an electron e.

Since two different sets of collimating apertures were used for the two angular ranges, the scattered currents were divided by the $G_{AVG}(\theta)$ appropriate to the set of apertures used before normalization. Normalization, then, at 1.5° yielded absolute cross sections throughout the 0.5°-5.0° range. As mentioned in the previous section, H^- was a negligible influence on the measurement of H^+.

Detection of Scattered Metastables

Relative angular distributions of scattered H(2s) were measured for constant energy, beam intensity, and target density. The detected metastable signal was determined by applying a quench voltage and

measuring the difference in signal with pre-quench voltage off and on. The background signal (i.e., signal due to collisions with the background gas) was determined in the same manner with no target gas in the collision cell. The net count rate N_s^{2s} is given by

$$N_s^{2s} = \{N\ (V_{pq} = 0) - N\ (V_{pq} > 0)\}\ p>0$$

$$- \{N\ (V_{pq} = 0) - N\ (V_{pq} > 0)\}\ p = 0 \qquad (20)$$

where V_{pq} is the pre-quench voltage and p is pressure of the gas target.

Angular distributions were measured in the 0.2°-1.5° range; for the 0.2°-0.5° range only relative distributions were measured, while for 0.5°-1.5° the relative data were converted to absolute cross sections.

Absolute Calibration

The cross section $I^{2s}(\theta_c)$ is given by

$$I^{2s}(\theta_c) = \frac{N_s^{2s}}{D_e\ N_B\ N_T\ G_{AVG}(\theta_c)} \qquad (21)$$

where D_e is the collection efficiency of the detection system.

D_e is dependent on (1) the distribution of photons (polarization) emitted during stark quenching of the scattered H(2s) atoms, (2) the solid angle subtended by the detector, (3) the transmission of the two grids, (4) the transmission of LiF filter, and (5) the quantum efficiency of the channeltron funnel. For nonisotropic photon emission the measured cross section, σ_M, is related to the

true cross section, σ_T, by the relation

$$\sigma_T = \frac{3 - P}{3(1 - P \cos^2 \theta)} \sigma_M \tag{22}$$

where θ is the direction, with respect to the electric field, viewed by the detector, and P is the polarization given by

$$P = \frac{I_{||} - I_{\perp}}{I_{||} + I_{\perp}} \tag{23}$$

where $I_{||}$ and $I_{\perp}$ are the intensities of radiation parallel and perpendicular to the field direction when the detector is set to $\theta = 90°$. This polarization correction, however, requires knowledge of the entry time of the H(2s) into the quenching field. Since the quantum efficiency is not known for the channeltron used in the present experiment (and since efficiency has been shown to vary over long periods of time, requiring numerous recalibrations) the detection efficiency was not determined directly. Instead, a normalization procedure was utilized.[29] Briefly, the experiment was prepared for measuring the total cross section for the charge transfer process

$$H^+ + Ar \rightarrow H(2s) + Ar^+ \tag{24}$$

at 20 keV. This simply required the removal of the scattered flux collimators. The data was then normalized to an absolute measurement made by Andreev et al.,[30] thereby establishing a value for D_e.

Since the calibration was made at only one energy (20 keV) it was necessary to ascertain that the detection efficiency was energy

independent throughout the energy range of this experiment (1 - 20 keV). A possible energy dependence would be manifested through a variation in the distribution of Lyman-alpha emitters in the detection region. The number of emitters (in this case H(2s) atoms) as a function of position, x, along the particle trajectory where x = 0 is the edge of the grounded shield (i.e., the point at which the quench field begins) is given by

$$N_s^{2s}(x) = N_s^{2s}(0)\ e^{-x/v\tau} \tag{25}$$

where v is the velocity of the emitter and τ is the H(2s) lifetime (dependent on the strength of the applied quenching field).

The distribution of emitters is unchanged for constant $v\tau$; thus at a given velocity, $v = \sqrt{2E/M}$, the quenching field, F, is appropriately chosen so that product $v\tau$ is constant. It has been shown that the field dependence of the transition rate, $W_{2s}(F)$, (in the case of two states, $2s_{1/2}$ and $2p_{1/2}$) is given by

$$W_{2s}(F) = \frac{1}{\tau_{2s}} = 3.12 \cdot 10^8 \left\{1 + \frac{\delta^2}{\left[1-(1+\delta^2)^{1/2}\right]^2}\right\}^{-1} \text{sec}^{-1} \tag{26}$$

where $\delta = F/237$

$$\cong 2720\ F^2\ \text{sec}^{-1} \tag{27}$$

for small F (i.e., $F \lesssim 100$ V/cm) and is shown in Figure 9. The ratio of the count rate at this field strength to the count rate at a saturation field F_s (the field at which better than 98% of the

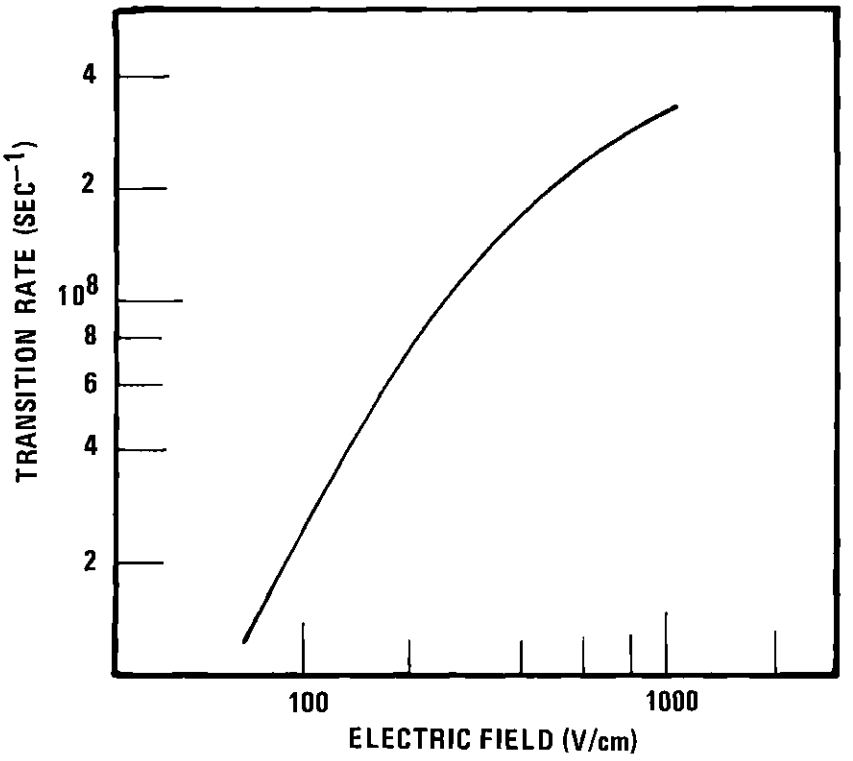

Figure 9. Transition Rate as a Function of Electric Field Strength for H(2s) Atom.

metastables have decayed in the detection region, approximately 600 V/cm at 20 keV) was compared at energies from 1-20 keV. No change to within ±5% in the ratio was observed indicating the detection efficiency was constant.

Monitor of D_e

The calibration described above required the removal of the collimating apertures, a procedure resulting in the exposure of the channeltron to atmospheric pressure while the vacuum system was exposed to air. The following method[31] was employed for monitoring the value of D_e without resort to recalibration.

Immediately after the calibration (without angle defining apertures), Ar was admitted into the main chamber at pressures ranging from $0.5 \cdot 10^{-6}$ to $5.0 \cdot 10^{-6}$ Torr. With the quench voltage set equal to zero, a beam of protons created collisions within the Lyman-alpha detector's viewing area, resulting in the formation of H(2p) yielding, upon decay to the ground state, Lyman-alpha radiation. A change in the variation in photon count rate (normalized to beam intensity) versus pressure reflects a change in detection efficiency. Knowledge of the relationship, K, between the slope of the pressure plot with D_e provided a means of redetermining the value of D_e in subsequent measurements (with collimating apertures replaced) without recourse to recalibration.

Total Cross Section

In addition to the previously described scattered particle measurements, the total cross section for

$$H(1s) + He \rightarrow H(2s) + He \tag{28}$$

was measured directly by removal of the angle determining collimating apertures. Metastable hydrogen atoms scattered from 0.0 to $\pm 7.0°$ could be detected. From the angular distribution, it was shown that metastables scattered beyond this angle contributed less than 0.1% to the total cross section. This then allowed for the collection of effectively all the metastables formed in the collision.

The metastable signal determined by

$$N^{2s} = N\ (pq = 0) - N\ (pq > 0) \tag{29}$$

was measured at numerous pressures varying from zero to 0.1 micron. (The limit of 0.1 micron was necessitated to (1) minimize the rise in base pressure of the main chamber and (2) to restrict the signal count rate to under 1000 $^{counts}/_{sec}$). The total beam flux was measured simultaneously by the Faraday cup at the end of the detector assembly. The total cross section is given by

$$\sigma_{2s} = \frac{N^{2s}}{D_e\ N_T\ N_B\ L} \tag{30}$$

where L is the cell length (see discussion of pressure profile). The value for N^{2s}/N_T was determined from the slope of the signal versus pressure curve.

CHAPTER IV

ERROR ANALYSIS

Introduction

Before presentation of the experimental results, it is necessary to accumulate all the errors associated with each cross section so as to establish limits on the reliability of the data points. In the following sections each parameter that participates in the calculation of the differential cross section (defined in Appendix A) and total cross section (defined in Chapter III) will be assessed with respect to the errors that contribute to its accuracy limit.

In most cases the measurement of a given parameter involves both random errors and systematic errors. Random errors can best be described as either (1) the result of measurements which are not exactly repeatable due to fluctuating conditions (such as projectile beam instability, temperature variations, etc.), or (2) the result of measurements which by nature are statistical. Systematic errors, however, normally arise from the accuracy limitation inherent in a given measuring instrument. Also, a systematic error in a certain parameter may be the resultant of both random and instrumentation errors occurring in the measurement of quantities which enter into the determination of that parameter. In general, for differential cross sections only random errors contribute to the relative distribution as a function of angle (except for systematic errors which are angle dependent, such as the determination of θ_c).

For each parameter, the total error is determined by computing the square root of the sum of the squares of all the contributing errors[33] whether they be random or systematic--likewise, the differential and total cross section will have total errors which are computed in the same manner from the total errors in each parameter.

Error in Beam Flux, N_B

The projectile beam flux measurement requires knowledge of the secondary emission coefficient, γ°, for the Faraday cup located in the target cell. This is determined from the measurement of γ^+ and knowledge of γ°/γ^+.

Error in γ^+

The determination of γ^+ is found from a measurement of an H^+ current, i^+, (for given projectile energy) and i_T (see Chapter III), both of which have errors due to beam instabilities (random). Since the measurement of both currents can be done quickly (although not simultaneously), no more than a $\pm 2\%$ change in ion intensity was observed during their measurement. Only the ratio of i_T to i^+ is necessary to the determination of γ^+; hence the accuracy limitation of the micromicroammeter is unimportant. The total error in γ^+ is assessed to be $\pm 2.8\%$.

Error in γ°/γ^+

The value of γ°/γ^+ (the ratio of secondary emission coefficients for the impact on a metal surface for a neutral atom and its ion) has been determined independently by numerous groups in the energy range of the present experiment. An average of the errors associated with

each determination of $\gamma^{\circ}/\gamma^{+}$ yields a probable error of $\pm 5.0\%$, which is considered a systematic error in the determination of N_B.

Total Error in N_B

During the measurement of the differential and total cross section the H° beam intensity was stable to $\pm 3\%$ (random error). The resultant uncertainty computed from this error plus the systematic errors in γ^{+} and $\gamma^{\circ}/\gamma^{+}$ is $\pm 5.7\%$.

Error in Target Density, N_T

The target density is computed directly from the pressure in the collision cell (see Chapter III). The errors in the determination of pressure arise from (1) the accuracy limit of the measuring instrument (MKS Baratron, cf. Chapter II), (2) pressure fluctuations, (3) shift in the zero of the Baratron meter, and (4) temperature variation in the pressure sensing head of the Baratron.

Manometer Accuracy

The pressure sensor had been calibrated against a McCleod gauge,[24] showing the device to be accurate to $\pm 5\%$ in the pressure range of the present experiment. As previously mentioned, the measured pressure has been corrected for thermal transpiration.

Zero Drift

The meter from which the pressure reading was made had fluctuations in its zero setting. The zero was found to vary ± 0.05 micron when the meter was set to the 1.0 micron range. Thus, for an operating pressure of 0.5 micron a random error of $\pm 10\%$ is present in the measurement. This drift occurred over a period of ~5 minutes; however,

over a period of ~30 seconds this drift was only ±.01 micron. The automatic valve switching system described in Chapter III allowed one to check the meter zero within seconds of making a determination of the pressure. Therefore the random error is reduced to a maximum of ±2%.

Temperature Fluctuation

The capacitance manometer sensor was designed by the manufacturer to operate at an elevated temperature (120°F) so that it could be temperature controlled. This required the following thermal transpiration correction[34]

$$P = \sqrt{\frac{T_{Room}}{T_{Sensor}}}\, P_{Reading} \tag{31}$$

where T is the temperature. Since the sensor is normally operated at ~120°F the correction is a 4% downward shift in pressure; this correction was made for the present data. Variations in temperature, both for the room and the sensor is estimated to produce a maximum variation in pressure of approximately ±1.0%.

Total Error in N_T

The errors in N_T are then ±2% random and ±5.1% systematic, resulting in a total probable error of ±5.5%.

Error in Scattered Proton Flux, N_S^+

Since the H^+ ion flux is measured directly as a current for $\theta_c < 1.5°$, the only errors that occur are errors resulting from projectile beam instabilities (random error) and the accuracy

limitation of the current measuring instrument (systematic error). The random fluctuations were assessed to account for $\pm$3.0% error, while the Cary electrometer was calibrated to be accurate to within 3.0%. The net error is calculated to be $\pm$4.5%.

The proton flux, for $\theta_c > 1.5°$, was measured by particle detection (see Chapter III). In this angular range the data was relative, i.e., the count rate was measured as a function of angle without any attempt to make an absolute determination of H^+ ion flux intensity. Since the counting rate was generally large ($\gtrsim$ 2000 counts per data point) the statistical (or random) error is ~$\pm$2%, which is in addition to the $\pm$3% due variation in beam intensity. No appreciable systematic error is assessed in this angular range. An absolute magnitude was placed on the data by virtue of normalization at 1.5° to the 'current measured' data which has an error bound of $\pm$4.5% associated with it. The total error in scattered H^+ for $\theta_c > 1.5°$ is computed to be $\pm$5.7%.

Error in Scattered Hydrogen Flux, N_S^o

The method for determining the scattered H^o flux is similar to that for the primary beam flux, i.e., γ^+ is measured and then multiplied by the ratio γ^o/γ^+. The current of secondary electrons from scattered neutral impact with the base of the detector is divided by the coefficient, γ^o. The only difference is that the detector is set to some large scattering angle (large in this case implies any angle for which the detector does not intercept the incoming projectile beam). This is required since the secondary electron emission coefficient is different at large angles than near $\theta_c = 0$ (see

Chapter III). Thus, at large angles, the scattered flux consists of H^+ as well as H^o. The measurement of γ^+ then requires a measurement of three currents: the H^+ ion current, the secondary electron current due to H^o impact, and the total current comprising the ion current plus the secondary electron current due to both ion and neutral impact.

Error in γ^+

The random error in γ^+ results from fluctuations in beam intensity occurring between measurements of the three currents described above; thus a random error of $\pm 2\%$ is ascribed to i^+, i^o, and i_T. The meter accuracy is assessed to be of little consequence since it is the ratio of $(i_T - i^o)$ to i^+ that enters into the determination of γ^+; this error is then considered to be zero. No systematic error contributes to the measurement of γ^+. The total error then in γ^+ is $\pm 3.5\%$.

Error in γ^o/γ^+

For a given impact energy the value of γ^o/γ^+ is identical to that used in the determination of N_B. Hence the total error associated with γ^o/γ^+ is $\pm 5.0\%$.

Total Error in N_S^o

The angular distribution of scattered neutrals requires a measurement of the secondary electron current I^o as a function scattering angle. The random and systematic errors are due to beam fluctuations and meter accuracy respectively; these are assessed to be $\pm 3\%$ and $\pm 2\%$. The total uncertainty, including errors in γ^+ and γ^o/γ^+ is computed to be $\pm 7.1\%$.

Error in Scattered H(2s) Flux, N_s^{2s}

Errors that contribute to the overall accuracy of the H(2s) signal measurement are due to (1) statistical fluctuations, or (2) loss of metastable hydrogen due to either field or collisional quenching prior to the detection region.

Random Error

The rate of detection of Lyman-alpha photons is statistical by virtue of the fact that probabilities are associated with emission of the photon from the excited atom and with the direction of the emitted photon. These result from the quantum mechanical nature of spontaneous emission. Thus the rate of detection is not constant, necessitating the accumulation of enough counts to obtain sufficient statistical accuracy in arriving at an average count rate which is indicative of the true flux of metastable hydrogen atoms. Unfortunately, the flux intensity coupled with the extremely small detection efficiency (about one photon is detected per 10^5 H(2s) atoms) resulted in count rates of only 0.5 count/sec at scattering angles of only 1.5°. The statistical error is found by computing the fractional standard deviation defined by[35]

$$S_N = \frac{1}{\sqrt{N}} \tag{32}$$

where N equals the total number of accumulated counts. At least 1000 counts were collected at each data point (i.e., at each scattering angle), which yields an error of $\pm 3.2\%$. At times when counting rates were much higher more than 1000 counts were attained; however, the

error of ±3.2% will be used to serve as an outside statistical limit on the H(2s) data, both for differential and total cross sections. Since fluctuations in beam intensity also influence the measured count rate, this is considered an additional source of error estimated to be ±3%. The resultant random error is ±4.4%.

Quenching

Loss of metastable hydrogen before the scattered flux has reached the detector is due to two sources. (1) Electric fields present in the region between the entrance to the collision cell and the front of the metastable hydrogen detector and (2) collisions of H(2s) with other particles, thereby possibly removing H(2s) through excitation or de-excitation. For the case of field quenching corrections were made on N_s^{2s} to account for loss arising from a bias voltage in the target cell region. All other plates were grounded including a shield extending slightly into the detection region (see Chapter II) so that quenching due to the fringe field of the detector's quench field was small and corresponding H(2s) loss negligible. Collisional loss was also assessed to be negligible since N_s^{2s} varied linearly with target pressure, indicating that H(2s) atoms were not undergoing collisions. Therefore a 0.0% error is attributed to both loss mechanisms.

Cascade

An increase in Lyman-alpha signal can occur through spontaneous emission from higher excited states (principle quantum number, $n \geq 3$) formed in the collision. For the $n = 3$ level, which is considered the primary contributing quantum state, the only allowed transition to the $2s_{1/2}$ state is from the 3p sublevel. Total cross sections

measured by Orbeli et al.[6] for formation of H(3p) indicates that the Lyman-alpha signal in the present total cross section measurements are too high by approximately 10%. Since no measurements have been made thus far the differential cross section for formation of H(3p) it is difficult to properly assess the contributing error. Hence neglect of cascade will not be included in the total error. All cross sections are then properly interpreted as cross sections for total formation of H(2s). In the case of total cross sections the cross section for direct excitation is about 10% lower than the measured value.

Total Error in N_s^{2s}

The total uncertainty in the determination of Lyman-alpha emission is assessed to be $\pm$4.4%.

Error in H(2s) Detection Efficiency, D_e

The method of determining D_e is described in brief in Chapter III and in greater detail in refs. 20, 31. For total cross section measurement of H(2s) formed for the charge transfer collision for protons on argon. Since the angle defining apertures are removed, the errors incurred in the determination of D_e are directly applied as systematic errors in total cross sections for the H(2s) excitation collision. However, the situation is not so simple for the case of angular scattering in which D_e must be determined twice (see Chapter III for the procedure utilized): (1) a direct measurement without apertures and (2) an indirect measurement of three quantities (1) D_e--without apertures, (2) an efficiency monitor K--without apertures, and (3) efficiency monitor K--with apertures) each of which containing

an associated error are required. Since these are independent measurements the errors are considered to be cumulative; hence, the error in D_e is larger for the 'scattered' H(2s) data than for the 'total' H(2s) data.

Error in D_e--Angle Defining Apertures Removed

Three measurements are required in determining D_e: (1) the total metastable flux, (2) the H^+ beam intensity, and (3) the target pressure. The statistical error in the metastable flux measurements is assessed to be $\pm$2% since generally ~2500 counts were accumulated. Randomness in the count rate due to beam fluctuations is not present since the two measurements were made simultaneously. The error in the H^+ beam intensity is due to beam fluctuations ($\pm$2%) and meter accuracy limits ($\pm$2%) resulting in a $\pm$2.8% error. Measurements of the Lyman-alpha signal were made at a number of pressures so that it was only necessary to know the difference in pressure accurately; thus, only $\pm$2% error due to zero drifts in the manometer readings was relevant. The net error from the three measurements is $\pm$4%.

The metastable signal divided by the beam flux and target density is normalized to the total cross section measured by Andreev et al.[30] to determine the detection efficiency D_e. Andreev's cross section measurement, however, has an error limit associated with it ($\pm$20%) and has an additional error of +6% to +18% due to the neglect of polarization of the field induced Lyman-alpha emission[36,37] (see Chapter III). If one considers the +6 to +18% error as a correction to the cross section measurement then it can be added to the $\pm$20% to give the largest possible error bounds; this yields an error of

-14% to +38%. The error in D_e is determined to be -14.8% to 38.2% when one includes the $\pm$4% error in the measurement of D_e.

Energy Dependence of D_e

A check on the variation in D_e as a function of projectile energy (see Chapter III) indicated that detection efficiency remained constant to within $\pm$5.0% throughout the energy range of the experiment.

Error in Efficiency Monitor K--Angle Defining Apertures Removed

In determining K (see Chapter III for description of procedure), measurements of Lyman-alpha intensity, beam intensity, and differences in gas pressure are required; the total uncertainty in the measurement of K is assessed to be $\pm$4%.

Error in Efficiency Monitor K--with Angle Defining Apertures

The measurement of K with collimating slits in place is identical to that made without apertures hence the uncertainty again is $\pm$4%.

Total Error in D_e--with Angle Defining Apertures

The error in D_e, which applies to the differential cross section data, is computed to be -16.6% to +39.0%.

Error in Geometrical Factor, $G_{AVG}(\theta_c)$

A full discussion of the manner in which the geometrical factor, $G_{AVG}(\theta_c)$ is evaluated is given in Appendix B. $G_{AVG}(\theta_c)$ is an explicit function of the scattering angle, θ_c; it also depends, implicit in its formulation, on slit widths (a and b), distance between the collision cell and the first slit (ℓ), distance between slits (H), slit height (h_s), beam width (w_B), beam height (h_B), and length of the collision cell (L).

The error in determining each parameter contributes, to some degree, to the final error in $G_{AVG}(\theta_c)$.

Error in Scattering Angle, θ_c

The method of determining the angle of scattering is discussed in detail in Chapter III. There it was pointed out that errors in determining $\theta_c = 0°$ and errors in reading the scale setting contribute to an uncertainty in θ_c: this uncertainty is angle dependent, i.e., the larger angles are known to a greater degree of accuracy than the smaller angles. The error in locating $\theta_c = 0$ on the steel rule (see Chapter III) was $\pm 0.02°$. The random error in making a visual observation of the scribe marks on the rule is $\pm 0.01°$. An additional error attributed to divergence of the projectile beam is 0.00° to -0.045°. The total uncertainty, then, in the location of the angle setting is -0.075° to +0.03°. Table 1 shows the appropriate percentage errors corresponding to the angular range of the differential cross section measurements.

The error in θ_c contributes to the cross section error in two ways: (1) directly, as an uncertainty in the angle for which the differential cross section was measured; (2) indirectly, by influencing the accuracy of the geometrical factor $G_{AVG}(\theta_c)$. The first contribution influences the cross section error by placing accuracy limits along the abscissa, while the second contribution is an added error to the ordinate for a plot of differential cross section versus scattering angle.

Table 1. Possible Error in Scattering Angle

θ_c	Upper Bound	Lower Bound
0.20°	+15.0%	-37.0%
0.25	+12.0	-30.0
0.30	+10.0	-25.0
0.35	+ 8.6	-21.4
0.40	+ 7.5	-18.7
0.45	+ 6.7	-16.6
0.50	+ 6.0	-15.0
0.60	+ 5.0	-12.5
0.70	+ 4.3	-10.7
0.80	+ 3.8	- 9.4
0.90	+ 3.3	- 8.3
1.00	+ 3.0	- 7.5
1.50	+ 2.0	- 5.0
2.00	+ 1.5	- 3.7
3.00	+ 1.0	- 2.5
4.00	+ 0.8	- 1.9
5.00	+ 0.6	- 1.5

Error in Slit Beam Dimensions, a, b, h_s, h_B, w_B

The widths and heights of both the beam collimators and the angle defining collimators were measured through the use of a telescope attached to the chuck of a milling machine; this permitted horizontal and vertical travel to an accuracy of 0.001 cm. However, visual observation of the edges of the collimating slits was only accurate to within 0.003 cm. The error in the slit dimensions was determined by making 10 measurements traveling from right to left across the slits and 10 measurements from left to right, and computing the standard deviation from the mean. Two sets of aperture sizes were utilized during the course of the experiment: the smaller set was necessary for attaining scattering angles smaller than 0.5°.

These apertures were also used for $\theta_c > 1.5°$. The errors in $G_{AVG}(\theta_c)$ due to errors in slit widths a and b were approximately $\pm 4.0\%$ and $\pm 1.0\%$ respectively for the large apertures, and $\pm 10.0\%$ and $\pm 2.0\%$ respectively for the smaller apertures. Errors in beam size produced negligible error in the geometrical factor, while the slit height error only accounted for an error of $\pm 0.7\%$. It should be noted that all of these errors tend to vary with scattering angle; however, the actual error will be used to compute final error in $G_{AVG}(\theta_c)$.

Errors in Slit Distances, ℓ, H

The accuracy of the dimensions ℓ and H were taken to be the tolerances incorporated in the design of the collimation assembly. Both quantities resulted in errors limits of $\pm 0.7\%$ and $\pm 1.5\%$ respectively in the geometrical factor.

Error in Cell Length, L

The target gas is primarily confined to the inner cylinder of the target cell (see Chapter II for description of target cell arrangement). However, gas streaming out the entrance and exit orifices effectively increase the cell length.

The cell length actually enters the geometrical factor as a cutoff when the collimating slits are set to an angle for which the scattering length that they define exceed the cell length. The error in L is assessed to be $\pm 1.0\%$, the value varying slightly with scattering angle.

Total Error in $G_{AVG}(\theta_c)$

In computing the total probable error in $G_{AVG}(\theta_c)$, it would be incorrect to consider the errors from all the parameters with equal

weight. For example, in the case of the beam width, w_B, neglect of w_B (i.e., $w_B = 0$) changes $G_{AVG}(\theta_c)$ by 1.0% hence a small error in w_B is unimportant. The most reliable approach, thus, is to vary each parameter through its error limits and observe the resulting variation in $G_{AVG}(\theta_c)$. The total error will be computed by taking the square root of the rum of the squares of the deviation in $G_{AVG}(\theta_c)$ due to each parameter error. Table 2 shows the upper and lower error bounds as a function of angle for both sets of apertures utilized in the experiment. As expected the errors become more asymmetric for the smaller scattering angles.

Table 2. Possible Percentage Error in $G_{AVG}(\theta_c)$

	0.25°	0.50°	1.00°	1.50°	2.00°	3.00°
Small Apertures	+10.2 to -13.1	+10.4 to -13.0	--	--	+10.6 to -11.2	+10.5 to -10.7
Large Apertures	--	+ 4.8 to - 7.1	+ 4.7 to - 6.6	+ 4.8 to - 6.5	--	--

Total Error in Total Cross Section, σ_{2s}

The errors incurred in the determination of the total cross section for formation metastable hydrogen is summarized in Table 3. The total uncertainty in σ_{2s} is found to be -18.5% to 39.8%. One should note than an error also exists in the determination of impact energy of the collision so that an error of $\pm$2.0% in the energy

ought to be considered in a curve which plots cross section versus energy.

Table 3. Possible Errors in Total Cross Section Measurement

	N_s	D_e	N_B	N_T	L
Percentage Error	$\pm$4.4	-15.6 to +38.5	$\pm$5.7	$\pm$5.5	$\pm$3.9

Total Error in Differential Cross Sections, $I^{2s}(\theta)$, $I^{o}(\theta)$, $I^{+}(\theta)$

Table 4 summarizes the total error in the differential cross section data at six different angles. It should be recalled that the scattering angles themselves have an associated error (Table 1). The error in relative distribution of the cross section is much less than the errors quoted in Table 4 since this error only arises from the error in $G(\theta)$ due to uncertainty of the scattering angle, and from the error in scattering angle. The uncertainty, then, in relative cross section is generally about $\pm$6%, varying slightly with angle.

Table 4. Possible Percentage Error in Differential Cross Section Data

θ	$I^{2s}(\theta)$	$I^{o}(\theta)$	$I^{+}(\theta)$
0.25°	+41.3% to -22.9%	+14.8% to -16.9%	+14.1% to -16.3%
0.50	+41.3 to -23.2	+14.9 to -16.8	+14.3 to -16.3
1.00	+40.3 to -20.1	+11.6 to -12.5	+10.8 to -11.8
1.50	+40.3 to -20.1	+11.7 to -12.5	+10.8 to -11.8
2.00	+41.4 to -22.0	+14.7 to -15.4	+14.1 to -14.8
3.00	+41.4 to -21.7	+14.7 to -15.1	+14.3 to -14.5

CHAPTER V

DATA

Total Cross Sections

Previous Work

Previous measurements of the total cross section for the collisional formation of H(2s) has been made by Orbeli et al.[6] in 1970 and by Birely and McNeal[7] and Hughes and Choe[8] in 1972. These authors have provided the only data directly applicable to the present total cross section measurements.

Orbeli measured the excitation cross section for H(2s), H(2p), and H(3p) at collision energies varying from 5-40 keV; the noble gases comprised the targets for this work. Projectile hydrogen was found by charge transfer neutralization of a proton beam. Although the Lyman-alpha intensity from H(2p) excitation could be measured directly, the H(2s) signal was obtained by subtracting the H(2p) signal from the Lyman-alpha intensity with a strong electric field (600-800 $^{V}/_{cm}$) which was the sum of the 2p and 2s emission. The absolute magnitude of the H(2p) cross section, $\sigma(2p)$ was determined by comparing the signal from the collisionally excited H(2p) with Lyman-alpha of H(2p) formed by charge transfer of H^+, for which absolute measurements were made. The absolute H(2s) cross section, $\sigma(2s)$ was determined from the ratio of H(2s) signal to H(2p) signal beam in neon. Following neutralization the exiting ions were electrostatically removed and metastable hydrogen atoms were field quenched. The projectile flux

was measured by a thermoelectric detector which was calibrated by an H^+ ion beam, for which the ion flux could be determined directly as a current; the efficiency for H^o was assumed to be equal to that of H^+. The detection of Lyman-alpha emission was made by a vacuum monochromator and photoelectric quantum counter which viewed the collision, giving $\sigma(2s)/\sigma(2p)$ and knowledge of the H(2p) cross section. Accuracy of the excitation data, then, is poorer than that for the electron capture data which was quoted to be accurate to $\pm$20%; error limits of $\pm$35% were placed on the H(2s) excitation measurements. No error estimate was made for the neglect of polarization of Lyman-alpha emission due to the presence of the quenching field. In addition to the H(2s) and H(2p) measurements Orbeli and coworkers measured the cross section for formation of H(3p) by measuring the intensity of Lyman-beta emission. Since a fraction (28%) of H(3p) spontaneously de-excite to the 2s state the H(3p) cross section gives an indication of the effect of cascade to the formation of H(2s); the contribution is approximately 10% for both the He and Ar targets. The data for helium and argon are shown in Figure 10.

Birely and McNeal studied excitation of hydrogen in collisions with rare gases for projectile energies varying from 1 to 25 keV. The projectile beam of H^o was also formed by charge transfer neutralization in argon. The H^o flux was measured by secondary electron detection. As in the experiment of Orbeli the Lyman-alpha emission originated from within the collision region. The detector consisted of a solar-blind photomultiplier, an O_2 filter with MgF_2 windows retractable SrF_2 filter, and a MgF_2 end window. This assembly viewed the emission at

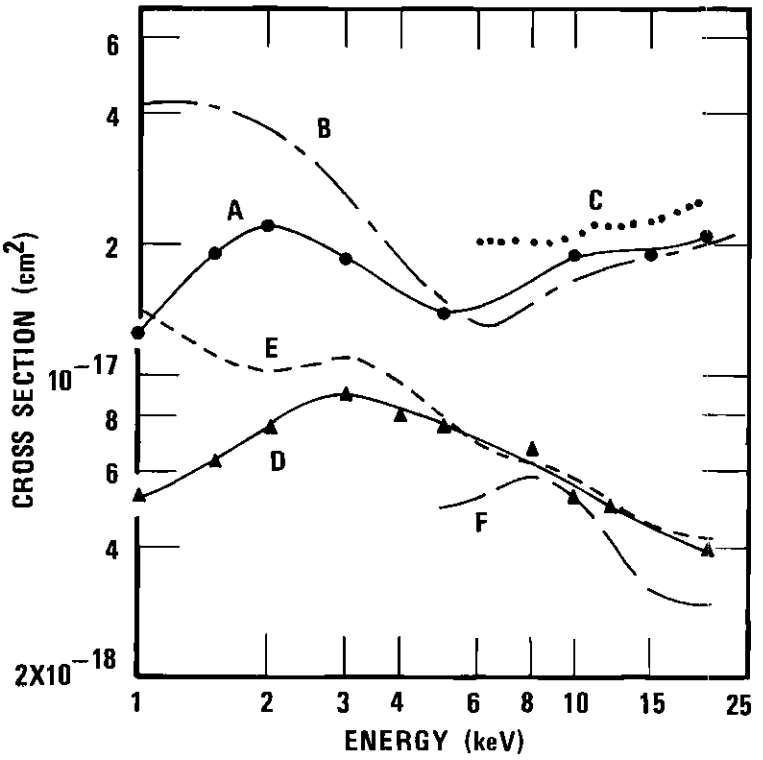

Figure 10. Total Cross Sections for Formation of H(2s). A. Present Data for Ar Target, B. Data of Birely and McNeal[7] for Ar Target, C. Data of Orbeli et al.[6] for Ar Target, D. Present Data for He Target, E. Data of Birely and McNeal for He Target, F. Data of Orbeli et al.[6] for He Target.

54.7°, 90°, or 125.3° with respect to the beam trajectory. The two non right-angle directions permitted the detection of polarization independent emission and permitted the comparison of this emission with that at 90°. However, it is not clear that the photon detection efficiency was independent of the beam energy.

Hughes and Choe[8] also measured the H(2s) cross section for He, Ne, Ar, and N_2 targets, but in a higher energy range (20-120 keV), so that comparison can only be made at the single energy, 10 keV, with the present results. The experimental method of Hughes and Choe is similar to that of the present work: fast protons are passed through a differentially pumped charge transfer cell to provide neutrals which then pass through a target cell, and finally H(2s) formed during the collision are detected beyond the target cell by field induced emission of Lyman-alpha radiation. The true H(2s) signal was distinguished from the background by taking the difference in signals with the quench field on and off, unlike the method of the present work which utilizes a pre-quench field (see Chapter II). The detection system was calibrated by normalization to cross sections measured by Pretzer[38] for Lyman-alpha formed in proton-rare gas collisions.

Present Results

Shown in Figure 10 are the total cross sections of the present measurements of formation of H(2s) compared with the data of Orbeli et al. and Birely and McNeal.

For the helium target both Birely and McNeal's data and the present data agree quite well in magnitude and general features in the energy range 4-20 keV. Orbeli's data are systematically lower

than the present results and show a maximum at 8 keV. Below 4 keV the present data diverge from Birely and McNeal, and differ by a factor of 3 at 1 keV collision energy; however, both sets of data indicate a peak at approximately 3 keV.

In collisions with an argon target the excitation cross section is higher by a factor of 2 above the helium data. The cross sections measured by Orbeli lie systematically above the present results and appears to invariant with energy. In the energy range 5-20 keV the data of Birely and McNeal are in good agreement with the present data; again, however, there is disagreement below 5 keV. Both Birely and McNeal's curve and the present curve confirms a minimum in the cross section near 6 keV, while the present data also indicates a maximum at 2 keV.

In comparison with Hughes and Choe's measurement at 20 keV, the agreement is within 20% for both the helium and argon target. If the two sets of data are normalized to each other at 20 keV for both helium and argon targets the cross section curves varies smoothly throughout the energy range 1-100 keV; thus Hughes and Choe's measurements are compatible with the present results.

Differential Cross Sections

Differential-in-angle cross sections for scattering of H(2s), H^{o}, and H^{+} at 10 keV impact energy with a helium target are shown in Figure 11. No previous measurements of these cross sections have been made; however, qualitative features of the present results will be given here.

The three cross section curves in Figure 11 are smoothly varying

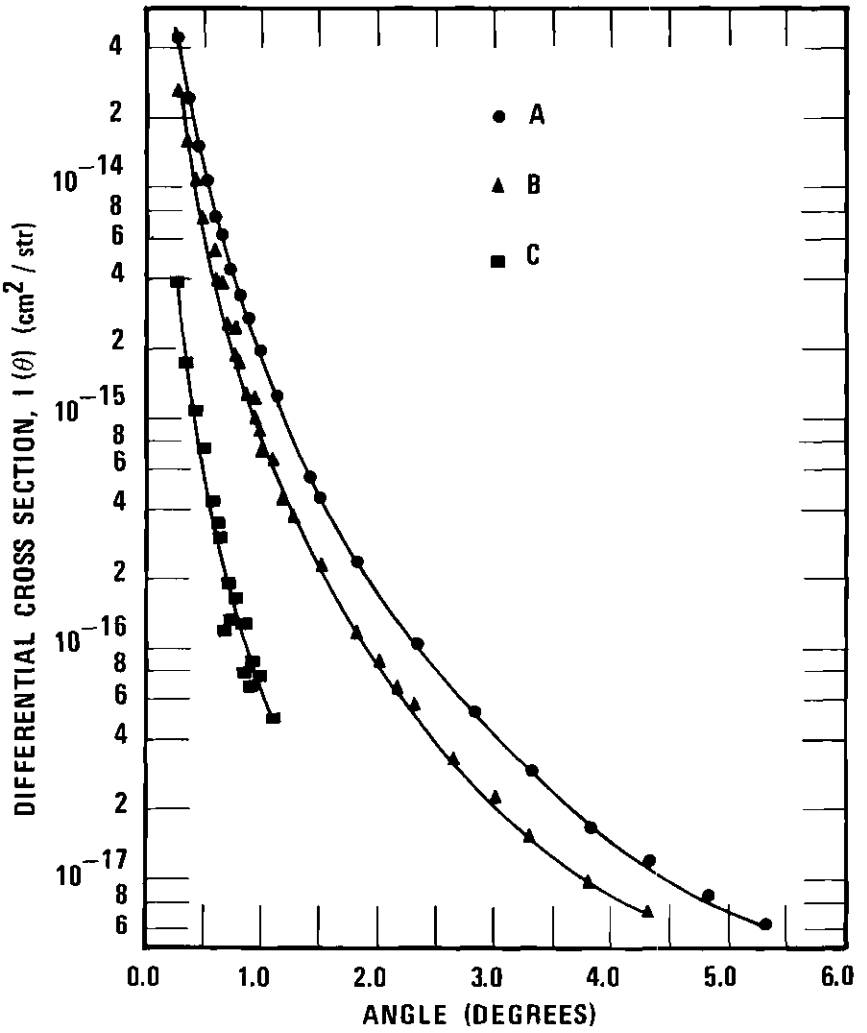

Figure 11. Differential Cross Sections for H(1s) + He Collision at 10 keV. A. Formation of H^+, B. Formation of H^0, C. Formation of H(2s).

functions of the scattering angle, θ, and they are nearly parallel throughout the angular range of the present measurements. For $\theta > 0.6°$, the data fit (in the least squares sense) functions of the form θ^{-n} where n = 3.2, 3.2, and 3.3 for H(2s), H^o, and H^+ respectively; below 0.6 these values of n diminish to 2.5, 1.9, and 2.2 respectively. The scattered H^o includes elastically scattered H^o and excited H^o. The fraction of metastable hydrogen formed is found by dividing the H(2s) cross section, $I^{2s}(\theta)$ by the H^o cross section, $I^o(\theta)$. The metastable fraction was relatively constant (0.08) for scattering angles larger than 0.6°, but at the lower end of the angular range (0.25°-0.6°) the fraction decreased from 0.15 at 0.25° to 0.08 at 0.6°. The differential cross section for ionization lies above the H^o cross section by about a factor of 2. It should be noted that cross section for ionization includes excitation to <u>all</u> continuum states, hence its rather large magnitude is not so surprising.

Other data, taken at 5, 15, and 20 keV impact energies, for scattering of neutrals and metastable hydrogen atoms are displayed in Figures 12 and 13 respectively. The angle scale in the two figures have been staggered so that cross section may be compared. Again the data (except for the 20 keV H(2s) curve for which there are few data points) displayed similar angular dependence to the 10 keV results. The metastable hydrogen content of the scattered neutrals is 0.07, 0.14, and 0.12 for 5, 15, and 20 keV respectively. Since most of the data was taken at only 4 impact energies (in 5 keV intervals) it is not possible to assess the variation of the cross sections with respect to energy with any precision. At any given angle of scattering the

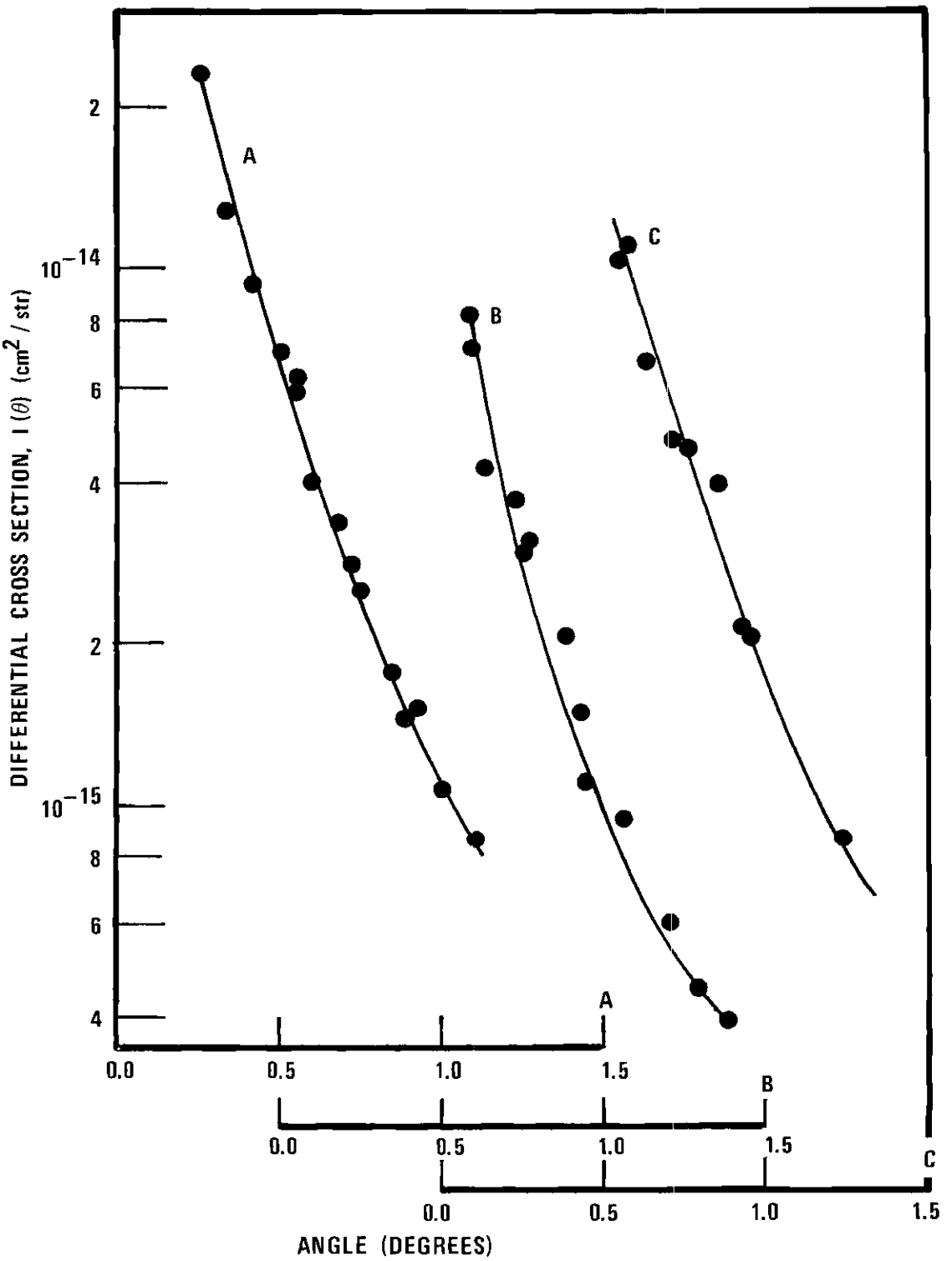

Figure 12. Differential Cross Section for H(1s) + He → H^{O} + He. A. 5 keV, B. 15 keV, C. 20 keV.

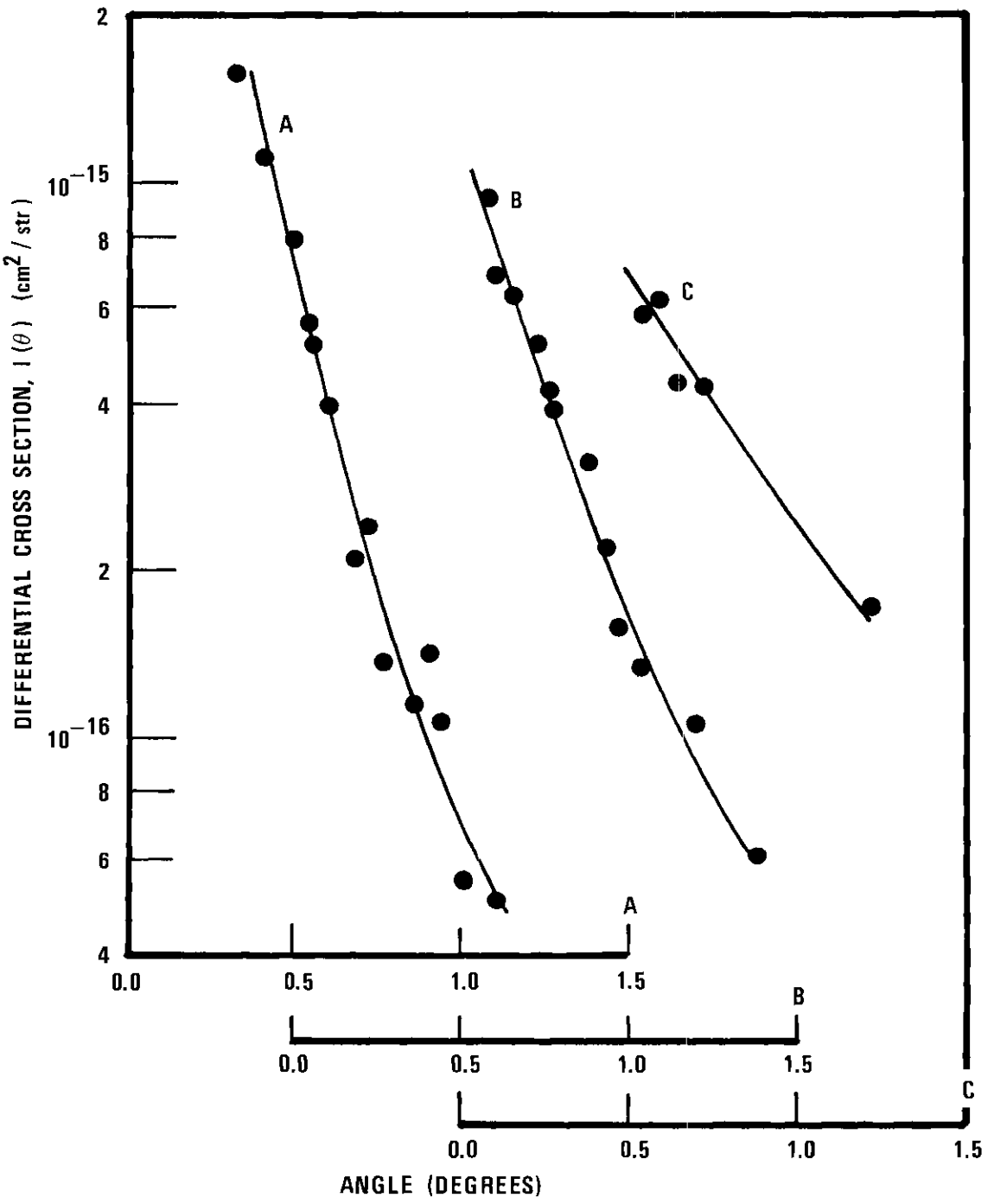

Figure 13. Differential Cross Sections for H(1s) + He → H(2s) + He. A. 5 keV, B. 15 keV, C. 20 keV.

magnitudes do not vary greatly; however, it is observed the cross sections (both for H^o and H(2s)) tend to decrease from 5 to 10 keV and to increase thereafter. To assess the importance of the angular range of the present measurements to the total scattering one can compute $2\pi\int_{\Delta\theta} I(\theta)\ \theta d\theta$ where $\Delta\theta$ is the angular range. For the 10 keV H(2s) data the integral is $\sim 1.5 \cdot 10^{-19}$ cm^2 which represents only 3.0% of the total cross section. This indicates that angles smaller than 0.25° influence the total cross section appreciably.

In addition to the measurements made at 5, 10, 15, and 20 keV, angular distribution of scattered H(2s) and H^o were measured at 1.5 keV and in the angular range of 0.20°-0.5°. Due to the experimental difficulty involved in obtaining these data the angular distributions are only relative measures of the differential cross section. Figures 14 and 15 show the variation with angle of the cross sections for H(2s) and H^o respectively. The curve in Figure 14 displays a strikingly different angular dependence than the cross sections in Figures 11, 12, and 13; a peak in the differential cross section is observed at 0.4° scattering angle. A further discussion of the structure at small scattering angles, in light of theoretical predictions, will be deferred until the next chapter. It should be noted, however, that the small angle structure is not due to the poor resolution which is inevitable at this range of angles. This is supported by the fact that the H^o cross section (Figure 15), measured at the same energy, decreases rapidly with angle.

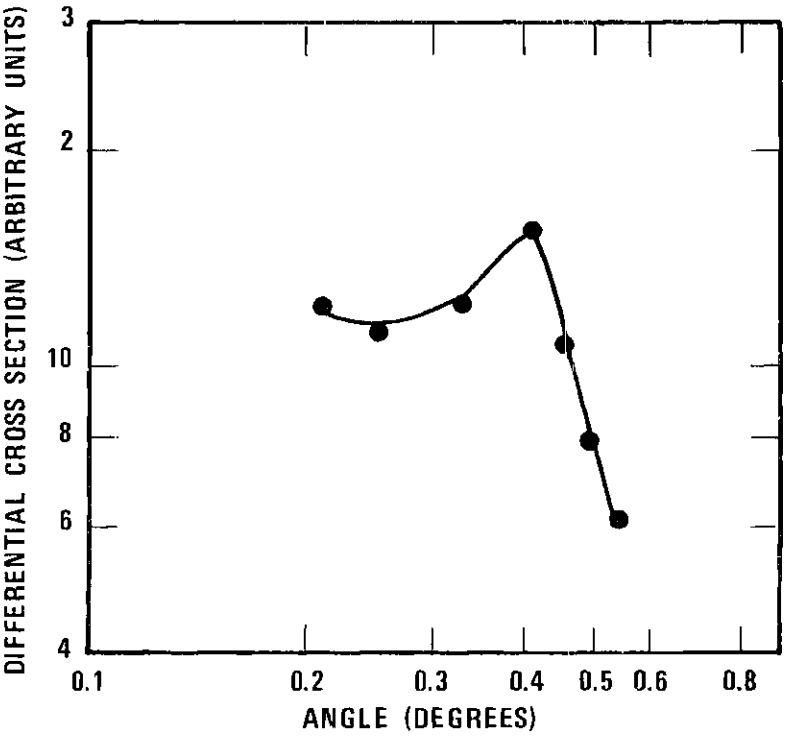

Figure 14. Relative Angular Distribution for H(1s) + He → H(2s) + He at 1.5 keV.

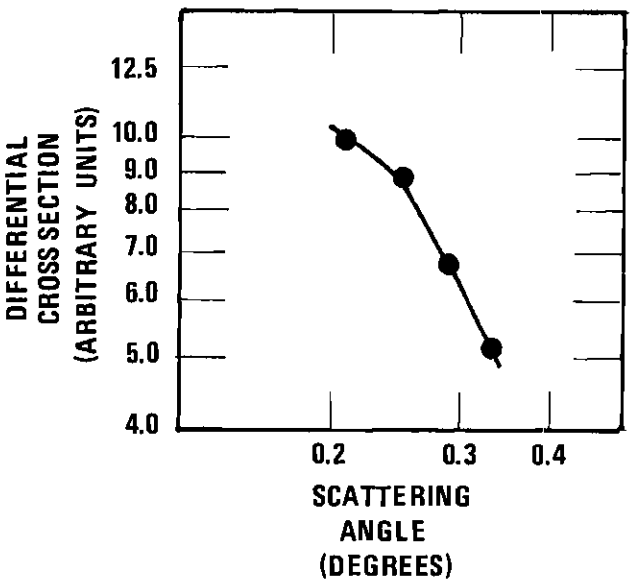

Figure 15. Relative Angular Distribution for $H(1s) + He \rightarrow (H^{O}) + He$ at 1.5 keV.

CHAPTER VI

THEORY--COMPARISON WITH EXPERIMENT

Introduction

In order to properly interpret the experimental results a number of theories will be described in relation to predictions of the total and differential cross section measured experimentally in the present work. A brief description of classical predictions of elastic scattering cross section is given, followed by an outline of various quantum mechanical theories which describe excitation in neutral-neutral collisions. It is not the intent here to present detailed derivation of the theory, but rather expose the reader to assumptions made in the theories in order to understand their validity. Comparison with the present data will be made whenever appropriate theoretical predictions exist. A few concluding remarks are then given in the final section.

Classical Theories

A classical treatment of the scattering problem requires knowledge of the interaction potential, U(R), of the colliding system. Generally the potential is simply a sum of the coulomb forces between the electrons and the nuclei. In collisions of heavy particles, the potentials may be approximated by simple expressions which utilizes screening distances to account for the presence of electrons in the atom (or ion). Once one decides on an appropriate U(R) the relationship between the scattering angle θ_{cm} (in the center of mass coordinate

system) and impact parameter, b, can be found by the equation[39]

$$\theta_{cm} = \pi - 2b \int_{R_o}^{\infty} R^{-2} \left[1 - \frac{U(R)}{E} - \frac{b^2}{R^2} \right]^{-\frac{1}{2}} dR \qquad (33)$$

where E is the collision energy and R_o is the distance of closest approach which is determined by setting the expression within the square brackets equal to zero. The differential cross section, $\sigma(\theta_{cm})$ can then be found from[40]

$$I(\theta_{cm})\ d\Omega_{cm} = \frac{b}{\text{Sin}\ \theta_{cm}} \frac{db}{d\theta_{cm}} \quad . \qquad (34)$$

The classically determined differential cross section can then be compared to data for 'total' scattered particles as a function of scattering angle. For the present work the 'total' differential cross section is found by adding the cross sections $I^o(\theta)$ and $I^+(\theta)$ (i.e., summing the two appropriate curves in Figure 11) which is represented by the reactions

$$H(1s) + He \rightarrow \begin{cases} H^o + He & (35) \\ H^+ + e + He \quad . & (36) \end{cases}$$

Potentials that have previously proved useful in predicting cross sections for ion-atom collisions are the screened-coulomb, screened shell, and static[41] potentials; brief descriptions of these will be given here.

Screened Coulomb Potential

The simplest model for collisions between atoms is through the use of a screened coulomb potential given in atomic units by[41]

$$U(R) = \frac{Z_1 Z_2}{R} e^{-R/a} \tag{37}$$

where Z_1 and Z_2 are the nuclear charges for the two colliding atoms (or ions), R is the internuclear separation, and $a = (Z_1^{2/3} + Z_2^{2/3})^{-\frac{1}{2}}$ is the electronic screening length. It is easy to see that this form of the interaction potential cannot distinguish between the collisions A + B, A^{n+} + B, and A^{n+} + B^{m+}. In the case of H + He, where the difference between the projectile (hydrogen) ion and atom is the most severe, this approximation is not expected to yield good results. This is confirmed by the fact that the 'total' differential cross section (at 10 keV) of the present data lies approximately 25% below the cross section for H^+ + He measured by Fitzwilson and Thomas.[21]

Screened Shell Potential

Rice and Bingham[41] considered a potential of the form

$$U(R) = \frac{Z_1(R)\, Z_2(R)}{R} \tag{38}$$

where $Z_i(R) = \Sigma\, \alpha_j^i\, e^{-R/a_j^i}$, α_j^i gives the number of electrons in subshell j of atom j (or ion) i, and a_j^i is the screening length of subshell j for atom i. The screening length is determined by

$$a_j^i = \sqrt{\frac{I_o}{I_j^i}} \tag{39}$$

where I_o is the ionization energy for a hydrogen atom and I_j^i is the energy required to ionize an electron in subshell j in atom i. This potential reduces to the one proposed by Smith[42] if $Z_1(R) = Z_1$ (i.e.,

the projectile is just an atomic nucleus). In considering the potential as a sum of screening terms, the collision, in which the projectile and target atom penetrates each other's shell structure, requires a more realistic approach to the collision problem. Also the screened shell potential distinguishes between the H^+ and H projectile in encounters with helium.

Figure 16 shows a theoretical calculation performed by Bingham[59] using the screened shell potential for the hydrogen-helium collision at 10 keV impact energy. The experimental data (curve C) show fairly good agreement with the theoretical prediction convoluted into the apparatus geometry (curve B). Also from the screened shell potential one can obtain a reasonable idea of the relationship between the impact parameter and the scattering angle; this relationship for 10 keV is displayed in Figure 17.

Static Potential

An interaction potential which also takes into account the atom's (or ion's) shell structure was developed by Rice and Bingham[41] in which the electron densities of the colliding partner is determined from Hartree-Fock-Slater probability densities. The interaction potential takes the form

$$U(\vec{R}_2 - \vec{R}_1) = \iint \frac{\eta_1(\vec{r}_1)\ \eta_2(\vec{r}_2)}{|\vec{R}_2 - \vec{R}_1 + \vec{r}_2 - \vec{r}_1|}\ d\vec{r}_1\ d\vec{r}_2 \qquad (40)$$

where η_i is the charge density, $\vec{r}_i$ is the distance relative to atom (or ion) i, and $\vec{R}_i$ is the nuclear position of atom (or ion) i. The charge density is determined from radial wave functions using the

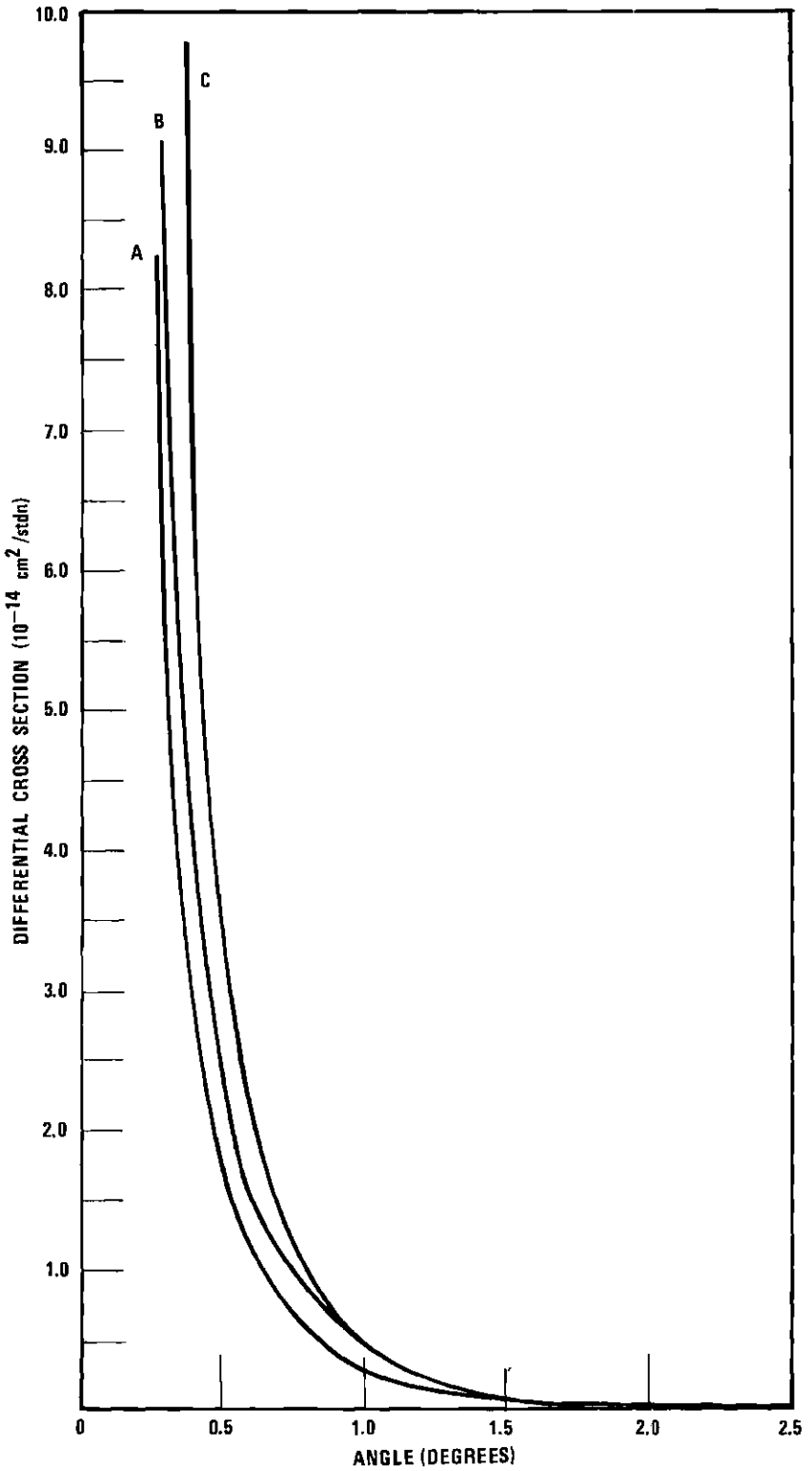

Figure 16. Differential Cross Section for H(1s) + He → H° + He Plus H(1s) + He → H^{+} + e + He at 10 keV. A. Screened Shell Potential, B. Curve A Convoluted into Apparatus Geometry, C. Present Data.

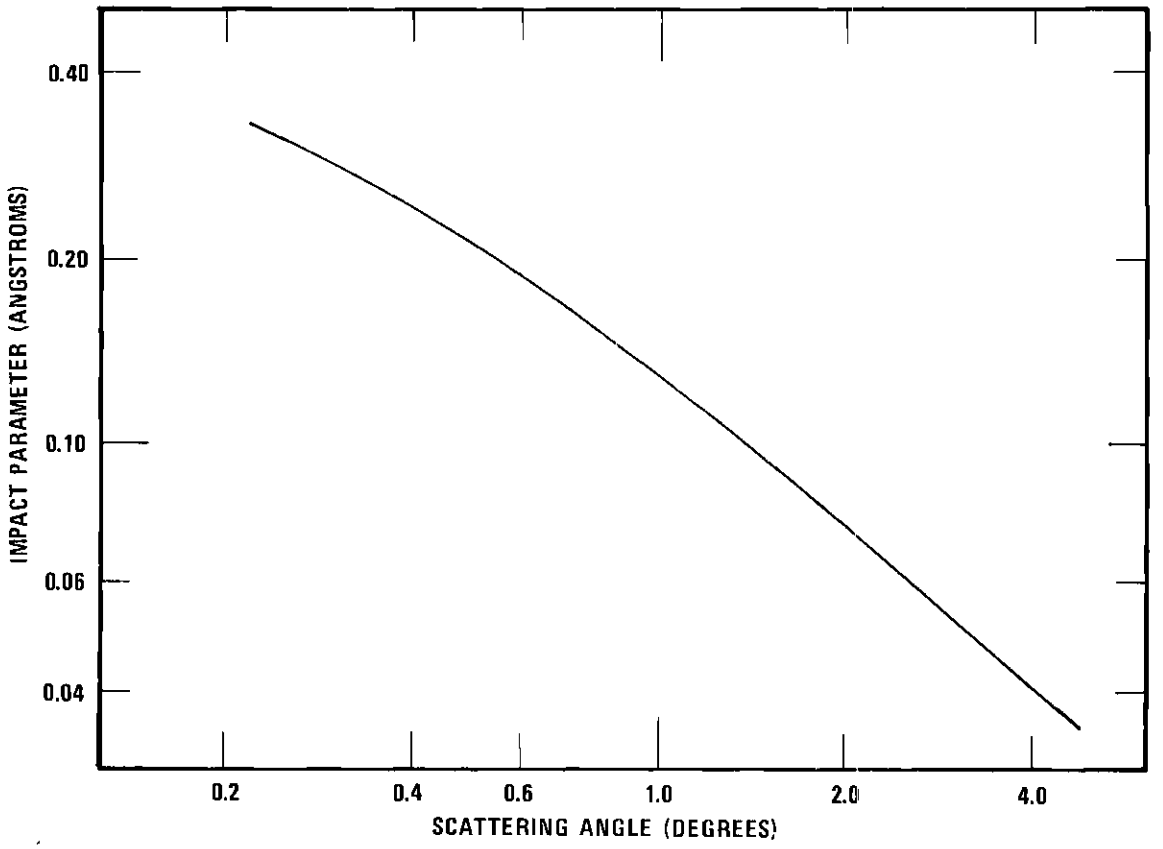

Figure 17. Impact Parameter as a Function of Scattering Angle for 10 keV H - He Collision.

Hartree-Fock-Slater self-consistent-field approximation. The potential effectively gives a more accurate picture of the electronic screening at all points along the projectile's trajectory. The method was shown to be quite successful in predicting the 'total' differential cross section for 10 keV H^+ collisions with helium (see Figure 26, Appendix B). At present, however, there are no available calculations of H + He collisions with the static potential.

Quantum Theories

Born Approximation

In order to obtain an exact quantum mechanical solution to the collision between atoms, A and B, one requires a solution to the Schroedinger Equation given by[44]

$$(\nabla_r^2 + k_n^2)\ \Psi_n(\vec{r}) = \sum_m U_{nm}\ \Psi_m(\vec{r}) \tag{41}$$

where $k_n^2 = 2m/h^2\ E_n$, $\Psi_n(\vec{r})$ describes the relative motion in state n and the matrix element, U_{nm}, is related to the projectile and target wave functions Φ_A and Φ_B and the interaction potential $V(\vec{r}_A, \vec{r}_B, \vec{r})$ by

$$U_{nm} = \int \Phi^*_{An}(\vec{r}_A)\ \Phi^*_{Bn}(\vec{r}_B)\ V(\vec{r}_A, \vec{r}_B, \vec{r})$$

$$\times\ \Phi_{Am}(\vec{r}_A)\ \Phi_{Bm}(\vec{r}_B)\ d\vec{r}_A\ d\vec{r}_B \quad . \tag{42}$$

The solution requires that Ψ_n have the asymptotic form[45]

$$\Psi_n \sim \frac{f_n(\theta,\phi)}{r} \exp(i\, k_n\, r) \quad , \quad n \neq 0 \tag{43}$$

so that the differential cross section $I(\theta,\phi)$ is found from the scattering amplitude $f_n(\theta,\phi)$ by the relation[46]

$$I_{on}(\theta,\phi)d\Omega = \frac{v_n}{v_o} \left| f_n(\theta,\phi) \right|^2 d\Omega \tag{44}$$

where o and n are the incoming and outgoing channels and v is the relative velocity. The infinite set of coupled differential equations of Equation 41 is insoluble; however, the first Born approximation reduces the infinite set to a single equation by assuming that U_{no} is the only non-zero matrix element. This results in a solution of an equation of the form

$$(\nabla_r^2 + k_n^2)\ \Psi_n(\vec{r}) = U_{no}\ \Psi_o(\vec{r}) \quad . \tag{45}$$

This approximation effectively requires that either[47]

(1) the interaction is weak, or
(2) the collision energy is high.

Solution to Equation 45 has been found for a number of excitation collisions[11] in which both the projectile and target wave functions were hydrogenic and hence well known.

Levy[13] in 1969 applied the first Born approximation to collisions between hydrogen and helium by using form factors to describe the target atom. Figure 18 shows a comparison of Levy's Born wave calculation of the total cross section for the excitation process in

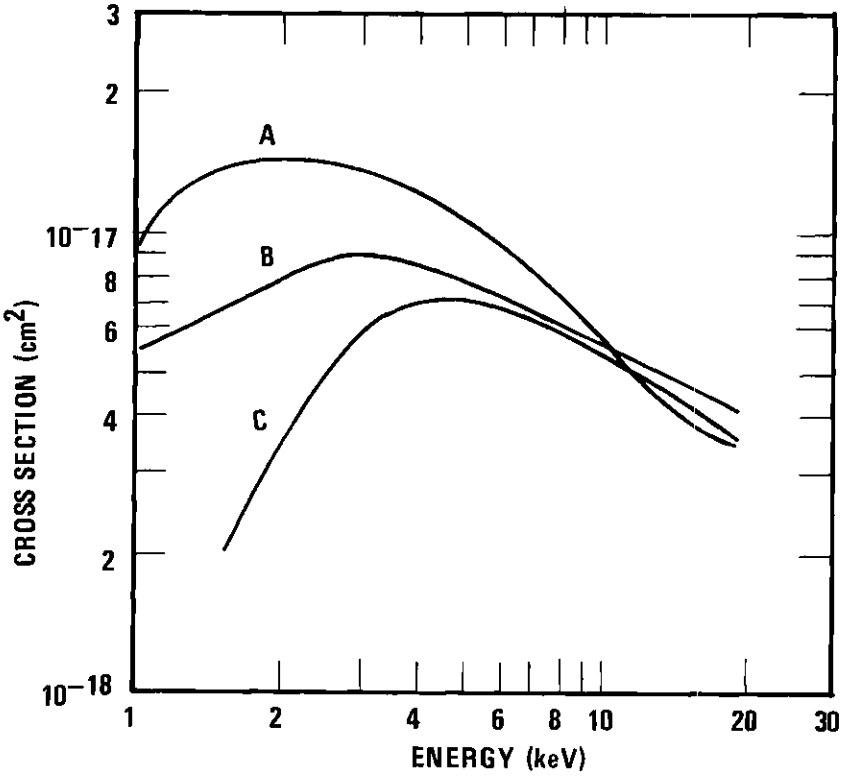

Figure 18. Comparison of Theory and Experiment for H + He → H(2s) + He. A. Born Approximation,[13] B. Present Data, C. Four State Impact Parameter Approximation.[17]

Equation (1) with the experimentally measured cross section. Agreement with the Born approximation is found for energies down to 10 keV. Recent measurements[48] of hydrogen excitation to the 2s state by helium ions differ from the Born approximation below 100 keV, indicating that short range forces of the neutral-neutral collision (satisfying requirement (2)) extends the validity of the Born approximation to much lower energies than for ion-atom collisions.

Shields and Peacher[18] in 1974 calculated the differential cross for reaction 1 from the first Born approximation. Their calculation at 10 keV impact energy[19] is shown in Figure 19 along with the experimentally measured differential cross section.* Here the Born approximation fails to predict the scattering cross section, indicating that a more sensitive test of the theory through the measurement of the differential cross section revealed the inadequacy of the theory whereas the total cross section obscured this fact in showing good agreement with the data.

From Equation 41 one can obtain an approximation less stringent than the first Born approximation by retaining all matrix elements involving only the initial and final states and setting the rest of the matrix elements to zero. The two resulting coupled equations are[50]

$$(\nabla_r^2 + k_n^2 - U_{nm})\ \Psi_n(\vec{r}) = U_{no}\ \Psi_o(\vec{r}) \qquad (46)$$

and

---

*The experimental data for this process has been converted to the center of mass frame from the data in Table 8 so that comparison can be made with theory.

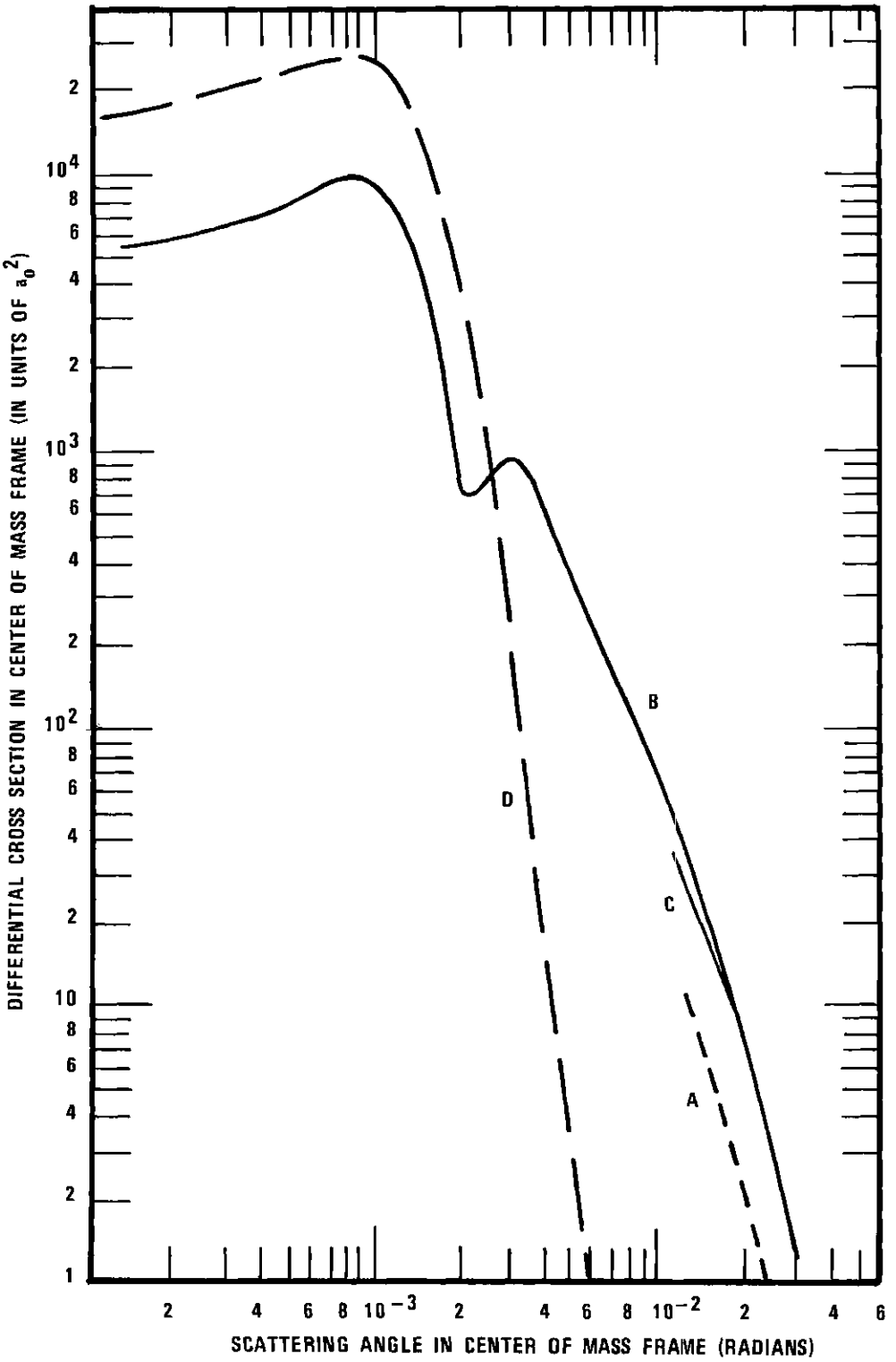

Figure 19. Comparison with Theory for Differential Cross Section of H(1s) + He → H(2s) + He at 10 keV. A. Present Data, B. Distorted Wave Born Eikonal Approximations,[19] C. Curve B Convoluted into Apparatus Geometry, D. Born Approximation.[19]

$$(\nabla_r^2 + k_n^2 - U_{oo})\ \Psi_o(\vec{r}) = U_{on}\ \Psi_n(\vec{r})\ . \qquad (47)$$

When one assumes that the term $U_{on}\ \Psi_n(\vec{r})$ is small compared to $U_{oo}\ \Psi_o(\vec{r})$, then when the right-hand side of Equation 47 is set to zero one obtains the distorted wave Born approximation. Bates[47] gives an analogous treatment using the impact parameter method to arrive at the distorted Born approximation. Again Levy[14] has applied this to the H - He collision. The results obtained were in very close agreement to theories based on the multistate models which will be described in the following section.

Multistate Treatment of Flannery and McCann

In general the exact form of the scattering amplitude $f_{if}(\theta,\phi)$ in terms of the interaction potential $V(\vec{r},\vec{R})$, the final total wave function Ψ_f is given by[51]

$$f_{if}(\theta,\phi) = -\frac{2\mu}{4\pi\hbar^2} < \Psi_f(\vec{k}_f\ ;\ \vec{r},\vec{R})\,|V(\vec{r},\vec{R})|$$

$$\times\ \Psi_i^{+}(\vec{k}_i\ ;\ \vec{r},\vec{R}) >_{\vec{r},\vec{R}} \qquad (48)$$

where the notation $< >_{\vec{r},\vec{R}}$ denotes integration over $\vec{r}$ and $\vec{R}$ (the electron motion relative to the center of mass and the relative nuclear motion respectively), and Ψ_i^{+} is the solution to the time-independent Schroedinger equation subject to the asymptotic boundary condition

$$\Psi_i^+(\vec{r},\vec{R}) \sim \sum_n \left\{ \left[e^{i\vec{k}_n \cdot \vec{R}} \delta_{ni} + f_{in}(\theta,\phi) \frac{e^{i k_n R_b}}{R_B} \right] \Phi_n(\vec{r}_a) \right\} . \qquad (49)$$

Through a series of approximations (outlined below) Flannery and McCann[52] have shown that the general scattering amplitude (Equation 48) reduces to the various Eikonal and impact parameter approximations which have been applied to neutral-neutral collisions.

To obtain the so-called Eikonal approximation the wave function $\Psi_i^+(\vec{r},\vec{R})$ is written in the form

$$\Psi_i^+(\vec{r},\vec{R}) = \sum_n A_n(\vec{\rho},z) \exp\{i S_n(\vec{\rho},z)\}\chi_n(\vec{r},\vec{R}) \qquad (50)$$

where $(\vec{\rho},z)$ define R in cylindrical polar coordinates and where the Eikonal is characterized by S_n when written as

$$S_n(\vec{\rho},z) = k_n z + \int_{-\infty}^{\infty} \left[\chi_n(\vec{R}) - k_n \right] dz' \qquad (51)$$

where

$$\chi_n(\vec{R}) = \left[k_n^2 - \frac{2\mu}{\hbar^2} V_{nm}(\vec{R}) \right]^{\frac{1}{2}} . \qquad (52)$$

Thus the wave function Ψ_i^+ is determined by an integration only along the Z direction which is the incoming trajectory of the projectile. More will be said about this later. The matrix element V_{nm} couples the wave functions χ_n and χ_m through the interaction potential by

$$V_{nm}(\vec{R}) = \langle \chi_n(\vec{r},\vec{R}) \, |V(\vec{r},\vec{R})| \, \chi_m(\vec{r},\vec{R}) \rangle \qquad (53)$$

where $\chi_n(\vec{r},\vec{R})$ is the product of the electron wave function $\Phi_n(\vec{r}_n)$ relative to the atom, and the plane wave $\exp(i\, mM_{AB}/M_A\, \vec{k}_n \cdot \vec{r})$ which describes the electron motion due to the atom's translation. In determining the coefficients $A_n(\vec{\rho},z)$, Flannery and McCann make the assumption that (1) $V_{nm}(\vec{R})$ varies slowly over many wavelengths of $2\pi/K(\vec{R})$ of relative motion, and (2) $A_n(\vec{\rho},z)$ vary only in the Z direction (the incoming projectile's direction). Thus, when the infinite number of channels is truncated to N, one obtains[52]

$$\frac{i\hbar}{\mu}\chi_f \frac{\partial A_f(\vec{\rho},z)}{\partial z} = \sum_{\substack{n=1 \\ \neq f}}^{N} \left\{ A_n(\vec{\rho},z)\, V_{fn}(\vec{R}) \times \exp(i(S_n - S_f)) \right\}. \quad f = 1,2,\ldots,N \tag{54}$$

Although the details of the derivation will not be given here Flannery and McCann have shown that the scattering amplitude can be given by

$$f_{if}(\theta,\phi) = -i^{\Delta+1} \int_o^\infty J_\Delta(K'\rho)\left[I_1(\rho,\theta) - i\, I_2(\rho,\theta)\right]\rho d\rho \tag{55}$$

where $K' = k_f \sin\theta$ and J_Δ are integral order Bessel functions and where

$$I_1(\rho,\theta\ ;\ \alpha) = \int_{-\infty}^{\infty} \chi_f(\rho,z)\, \frac{\partial c_f(\rho,z)}{\partial z} \exp(i\alpha z) dz \tag{56}$$

$$I_2(\rho,\theta\ ;\ \alpha) = \int_{-\infty}^{\infty} \left[\chi_f(\chi_f - k_f) + \frac{\mu}{\hbar^2} V_{ff}\right] c_f(\rho,z) \times \exp(i\alpha z)\, dz \tag{57}$$

and

$$\alpha = k_f (1 - \cos \theta) = 2k_f \sin^2 \frac{\theta}{2} \quad . \tag{58}$$

They also show that by assuming that (1) K_n is equal to the asymptotic value K_n and (2) the only non-negligible matrix elements are V_{ii}, V_{ff}, and $V_{fi} (= V_{if})$, one obtains the scattering amplitude

$$f_{if}^{DWB}(\theta,\phi) = - \frac{i\Delta\mu}{\hbar^2} \int_o^\infty J_\Delta(k_f \rho \sin \theta) \rho d\rho \int_{-\infty}^{\infty} V_{fi}(\rho,z)$$

$$\times \exp i[\{(k_i - k_f) + \alpha\}z + \Phi(z)]dz \tag{59}$$

where

$$\delta \Phi(z) = - \frac{1}{\hbar v_i} \int_{-\infty}^{z} V_{ii} dz' - \frac{1}{\hbar v_f} \int_{z}^{\infty} V_{ff} dz' \tag{60}$$

which gives the distorted wave Born Eikonal approximation of Chen, Jochain, and Watson.[53] In 1974 Peacher and Shields applied the method to hydrogen-hydrogen collisions[18] and recently[19] to hydrogen impact on helium. Differential cross sections for the excitation of hydrogen to the metastable state were calculated by this method and the theoretical results at 10 keV[60] is represented by the solid curve (A) in Figure 19. The agreement with experiment is significantly improved over the Born approximation. The angular dependence is in accord with the experimental data; however, the absolute magnitude differs by a factor of 4. The difference between the theory and the experimental data is not so severe when the data is compared with the convoluted theory and when the uncertainties (established in Chapter IV)

in both the absolute magnitude and scattering angle are imposed. For example at $\theta = 0.0125$ rad (center of mass) the minimum difference between experimentally determined cross section (when shifted upward by ~40% and to larger angles by ~15%) and the convoluted theoretical cross section is only a factor of ~1.7. The inclusion of the coupling terms $V_{1s,1s}$, $V_{2s,2s}$, and $V_{2s,1s}$ considerably improves the theoretical prediction of the differential cross section.

If Equations 55-58 are altered by the approximations (1) $\chi_f(\vec{R}) \approx k_f - \frac{\mu}{h^2 k_f} V_{ff}(\vec{R})$, (2) $k_f \approx k_i$, (3) $k_n - k_i \approx \frac{\varepsilon_{fi}}{hv_i}$, and (4) the scattering angle is small such that $\alpha \approx 0$, Flannery and McCann also show that the scattering amplitude becomes

$$f_{if}^{c(o)}(\theta,\phi) = -i^{\Delta+1} k_i \int_o^\infty J_\Delta(K'\rho)[C_f^c(\rho,\infty) - \delta_{if}]\rho d\rho \qquad (61)$$

where $K'^2 = K^2 - \frac{\varepsilon_{fi}}{h^2 v_i^2}$

and C_f^c satisfies the equation

$$i\hbar \frac{\partial C_f^c}{\partial z} = \frac{1}{v_1} \sum_{n=1}^{\infty} C_i^c(\rho,z) V_{fn}(\rho,z) \exp\left(\frac{i\,\varepsilon_{fn}\,z}{\hbar v_i}\right) \qquad (62)$$

where projectile velocity = $v_i = \frac{hk_n}{\mu}$. This is the <u>multistate impact parameter approximation</u>. Flannery and McCann[52] have also shown that the total cross section can be written as

$$\sigma_{if}(k_i) = 2\pi \frac{k_f}{k_i} \int_o^\infty |C_f(\rho,\infty) - \delta_{if}|^2 \rho d\rho \qquad (63)$$

when the high energy approximation $K'^2 \approx K^2 \approx 2k_1^2(1 - \cos\theta)$ and $\int_{k_i-k_f\approx o}^{k_i+k_f\approx\infty} J_\Delta(K\rho)\, J_\Delta(K\rho')K\, dK \approx \frac{1}{\rho}\,\delta(\rho - \rho')$ is applied to the scattering amplitude form of the total cross section given by

$$\sigma_{if}(k_i) = 2\pi \frac{k_f}{k_i} \int_o^\pi |f_{if}(\theta,\phi)|^2 \sin\theta d\theta \qquad (64)$$

In 1969 Flannery used the multistate impact parameter approximation to investigate the total cross section (Equation 63) for excitation of hydrogen in hydrogen-hydrogen[15,16] and hydrogen-helium[17] collisions. The four state approximation (incorporating the 1s, 2s, $2p_o$, and $2p\pm1$ states of hydrogen), from Ref. 17, for the helium target is compared in Figure 18 with the present experimental data (along with the comparison with the Born wave approximation). The agreement with experiment down to 4 keV impact energy is illustrative of the improvement of the multistate treatment over the Born approximation. Both the four state prediction and experiment display maxima near 4 keV. Below 4 keV, however, the two curves diverge. The inclusion of additional states in the expansion of Ψ_i^+ can conceivably improve the theoretical prediction for E < 4.0 keV. Also, electron exchange might be incorporated into the theory. Bottcher and Flannery[54] have already considered this for hydrogen-hydrogen collisions.

In 1973 Flannery and McCann[51] derived the form of the differential cross section using a multistate impact parameter description and performed calculations for hydrogen-hydrogen scattering[55] and hydrogen-helium scattering.[56] In the case of hydrogen-helium, their results are nearly identical to the prediction given by the distorted

wave Born Eikonal description. Thus there still remains a difference in magnitude between the predicted and experimental differential cross section for the multistate impact parameter treatment. A possible cause for the discrepancy may lie in the approximation made in the Eikonal, that is the assumption of a straight line trajectory. Since the projectiles are deviated somewhat, through the coulomb repulsion, a more accurate differential cross section would be obtained by considering a more realistic trajectory. The straight line trajectory will be adequate for "very small" scattering angles; however, what constitutes "very small" is not entirely obvious.

Both the multistate impact parameter approximation and the distorted wave Born Eikonal approximation exhibit interesting structure near $\theta = 0$ in the differential cross section. Unfortunately (from the experimental point of view) the relative maximum occurs below 0.1 degree in the 10 keV curve; it was not possible to reduce the beam and slit size sufficiently to attain such small scattering angles without completely eliminating the signal. Nevertheless it was noted that the maximum in the cross section appeared at larger scattering angles for lower impact energies.[56] Although the predictions (of total cross sections) of the two theories become less accurate as the collision energy is decreased, it was hoped that the general features of the differential cross section persisted at energies where agreement in magnitudes is not at all expected. With this in mind, calculations of the excitation cross section (Equation 1) at 1.5 keV impact energy, provided by J. L. Peacher,[60] is shown in Figure 20. In comparison the experimental results at this energy indicate a maximum in the

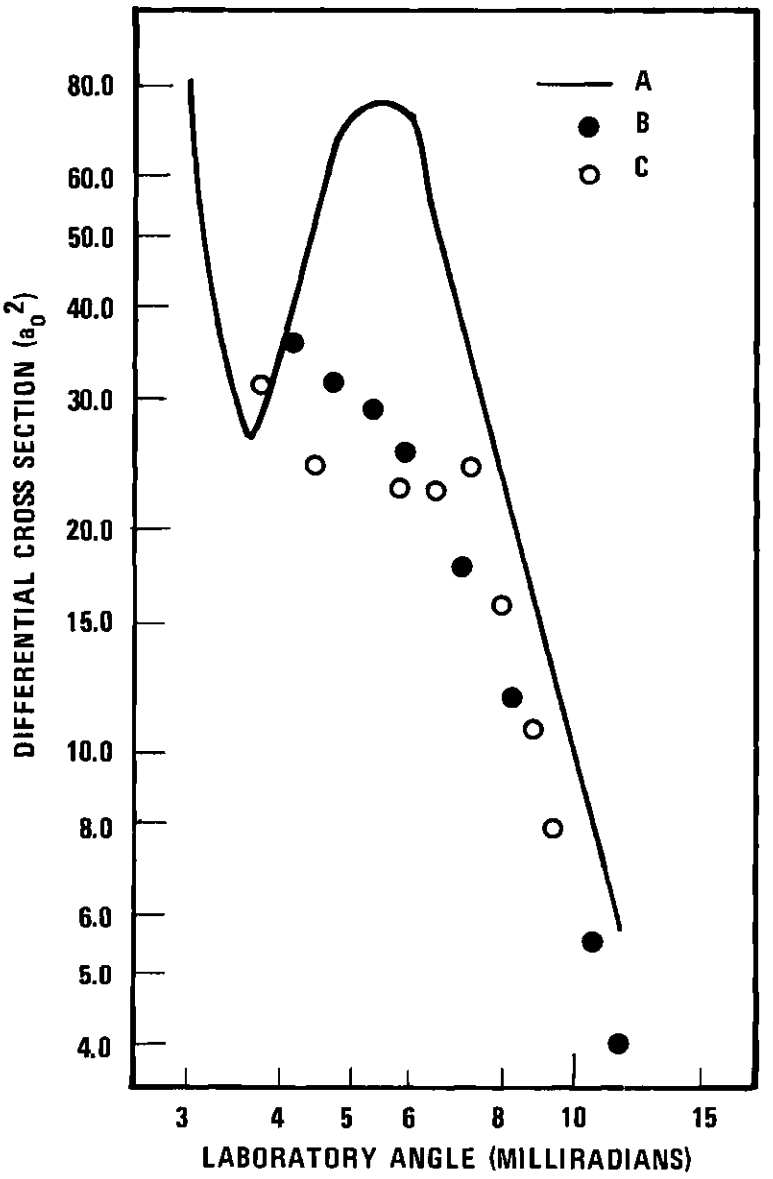

Figure 20. Comparison with Theory for Differential Cross Section of H(1s) + He → H(2s) + He at 1.5 keV. A. Distorted Wave Born Eikonal Approximation, B. Curve A Convoluted into Apparatus Geometry, C. Present Data Normalized to Curve B at $\theta = 0.53^{\circ}$.

differential cross section near the theoretical peak. Again the theoretical prediction was convoluted into the apparatus geometry to yield curve B in Figure 20; the data* (curve C) follow the convoluted theory surprisingly well. A physical interpretation of the structure remains subject to speculation.

Conclusions

In summarizing the results of the comparison between theory and experiment we can conclude the following:

1. For neutral-neutral collisions the Born approximation is valid (in the prediction of total cross sections) to an order of magnitude lower energy than for a similar ion-atom collision; however, the differential cross section remains in gross disagreement.

2. The four state impact parameter prediction of the total cross section for excitation of hydrogen in collisions with helium is in excellent agreement with experiment down to 4 keV collision energy, with both theory and experiment exhibiting similar peaks in the cross section.

3. Theoretical prediction (in either the distorted wave Born Eikonal or the multistate impact parameter description) of the differential cross section at 10 keV show good agreement in angular dependence while disagreeing in absolute magnitude. The difference might possibly be resolved by the theoretical inclusion of (a) additional coupling states, (b) electron exchange, and/or (c) a classical

---

*The experimentally measured differential cross section was normalized to the convoluted theory at $\theta = 0.53°$ in the laboratory frame.

trajectory to replace the assumed straight line path of the projectile.

4. Small angle structure which appear in the theoretical differential cross section appear to exist from a comparison with experimental measurements made at 1.5 keV impact energy.

APPENDIX A

DATA TABLES

Table 5. Total Excitation Cross Section, σ_{2s}, for H(1s) + He → H(2s) + He and H(1s) + Ar → H(2s) + Ar As Function of Energy, E

E(keV)	σ_{2s} (10^{-18} cm^2)
Helium Target	
1.0	5.25
1.5	6.15
2.0	7.54
3.0	9.00
4.0	8.10
5.0	7.60
8.0	6.84
10.0	5.10
12.0	5.01
20.0	4.02
E(keV)	σ_{2s} (10^{-17} cm^2)
Argon Target	
1.0	1.25
1.5	1.89
2.0	2.19
3.0	1.84
5.0	1.38
10.0	1.89
15.0	1.89
20.0	2.10

Table 6. Differential Cross Section, $I^o(\theta)$, for $H(1s) + He \rightarrow H^o + He$ As Function of Scattering Angle, θ. (Angles are in units of degrees; cross sections are in units of 10^{-15} cm^2/Steradian.)

θ	$I^o(\theta)$	θ	$I^o(\theta)$
E = 5 keV		E = 10 keV (continued)	
0.250	23.3	1.01	0.699
0.330	13.0	1.08	0.664
0.417	9.30	1.15	0.442
0.500	7.00	1.25	0.369
0.545	5.75	1.50	0.224
0.560	6.14	1.65	0.163
0.597	3.93	1.80	0.115
0.680	3.34	2.00	0.0881
0.727	2.82	2.15	0.0671
0.760	2.47	2.30	0.0572
0.847	1.72	2.65	0.0332
0.893	1.44	3.00	0.0225
0.930	1.48	3.30	0.0152
1.01	1.06	3.80	0.00951
1.10	0.850	4.30	0.00700
E = 10 keV		E = 15 keV	
0.250	25.8	0.580	8.15
0.330	16.0	0.587	6.89
0.417	10.6	0.625	4.10
0.500	7.5	0.718	3.61
0.575	5.29	0.755	2.89
0.597	4.04	0.763	3.10
0.608	3.90	0.875	2.03
0.675	2.52	0.920	1.45
0.742	2.37	0.958	1.09
0.775	1.74	1.04	0.912
0.763	1.80	1.21	0.587
0.842	1.26	1.29	0.440
0.908	1.21	1.38	0.391
0.925	0.973		
0.942	0.867		

Table 6. Concluded

θ	$I^{o}(\theta)$	θ	$I^{o}(\theta)$
E = 20 keV			
0.552	10.2		
0.572	10.8		
0.583	10.9		
0.635	6.55		
0.717	4.67		
0.750	4.61		
0.850	3.94		
0.917	2.10		
0.950	2.06		
1.22	0.850		

Table 7. Differential Cross Section, $I^+(\theta)$, for $H(1s) + He \rightarrow H^+ + e + He$ as Function of Scattering Angle, θ. (Angles are in units of degrees; cross sections are in units of 10^{-15} cm^2/Steradian.)

θ	$I^+(\theta)$
E = 10 keV	
0.250	44.5
0.330	24.0
0.417	15.0
0.500	10.5
0.583	7.40
0.617	6.10
0.717	4.40
0.795	3.40
0.883	2.65
0.965	1.95
1.12	1.27
1.42	0.560
1.50	0.450
1.83	0.235
2.33	0.102
2.83	0.0523
3.33	0.0288
3.83	0.0165
4.33	0.0120
4.83	0.00850
5.33	0.00620

Table 8. Differential Cross Section, $I^{2s}(\theta)$, for H(1s) + He H(2s) + He as Function of Scattering Angle, θ. (Angles are in units of degrees; cross sections are in units of 10^{-16} cm^2/Steradian.)

θ	$I^{2s}(\theta)$	θ	$I^{2s}(\theta)$
E = 5 keV		E = 15 keV	
0.333	15.8	0.580	6.84
0.417	10.2	0.587	9.55
0.500	7.90	0.625	6.22
0.545	5.54	0.718	5.13
0.560	5.10	0.755	4.17
0.597	3.94	0.763	3.78
0.680	2.04	0.875	3.13
0.727	2.38	0.920	2.18
0.760	1.34	0.958	1.55
0.847	1.12	1.04	1.32
0.893	1.41	1.21	1.05
0.930	1.04	1.29	1.29
1.01	0.530	1.38	0.590
1.10	0.500		
E = 10 keV		E = 20 keV	
0.250	39.0	0.552	5.84
0.333	17.5	0.572	6.01
0.417	10.6	0.635	4.22
0.500	7.40	0.717	4.34
0.575	4.35	1.22	1.78
0.597	3.44		
0.608	3.11		
0.675	1.91		
0.742	1.67		
0.763	1.32		
0.775	1.22		
0.842	1.33		
0.908	0.790		
0.925	0.860		
0.942	0.710		
1.01	0.780		
1.08	0.490		

Table 9. Relative Differential Cross Sections, $I^{o}(\theta)$ and $I^{2s}(\theta)$ for H(1s) + He → H^{o} + He and H(1s) + He → H(2s) + He, Respectively as Function of Scattering Angle for Very Small Angles ($\theta < 0.5°$). (Angles are in units of degrees; cross sections are in arbitrary units.)

θ	$I^{o}(\theta)$	$I^{2s}(\theta)$
	E = 1.5 keV	
0.21°	10.0	5.5
0.25	8.9	4.3
0.29	6.7	-
0.33	5.1	4.0
0.37	-	4.0
0.41	-	4.3
0.45	-	2.8
0.49	-	1.9
0.53	-	1.4

APPENDIX B

GEOMETRY FACTOR

APPENDIX B

GEOMETRY FACTOR

Introduction

In the present work experimental determination of differential (in angle) cross section are obtained by passing a beam of projectiles across a static target gas and recording the angular distribution of the emerging particles. The particle detector system inevitably subtends a finite solid angle at the target region so that the measurement provides a cross section value averaged in some way over the finite angular range encompassed by the detector. Few quantitative assessments have been made of how the finite resolution influences the measured data.

The objective here is two-fold: (1) to define the experimental differential cross section in terms of the measured quantities and apparatus dimensions, and assess various assumptions made in the derivation of the experimental cross section, and (2) to interpret the influence of the finite resolution on the theoretical microscopic cross section, particularly at small scattering angles (where the resolution is poor). In meeting objective (2) a specific example will be given, which illustrates from previously measured experimental data, how the theoretical cross section is distorted by the detection geometry.

Definition of Cross Section

First an expression must be derived that represents the cross section in terms of experimentally observed parameters. The customary procedure is as follows. Consider a beam of projectiles of flux N_B (particles/sec) with cross sectional area, A, and a target of density N_T (particles/cm^3). The flux of projectiles scattered into an element of solid angle $d\Omega$ from a volume element $d\tau$ of the beam path is related to the differential cross section, $I(\theta)$, by

$$d^4N_s = I(\theta) \frac{N_B N_T}{A} d\Omega \, d\tau. \tag{65}$$

In practice, a typical experiment uses a pair of defining apertures to select particles scattered into some small range of directions; the detection systems are then placed behind these apertures. Figure 21 illustrates the aperture system used for the present work. The angle between the original beam direction and the axis of the aperture system is designated θ_c. At the intersection of the aperture axis and beam line is an axis, perpendicular to the plane of the figure, about which the detection system is rotated when performing a measurement of the angular distribution; that intersection is also used as the origin of our co-ordinate system. It is clear from Figure 21 that at any point x on the beam path the apertures subtend some finite solid angle ω; moreover, particles may be scattered into the detectors from a wide range of positions on the beam path between x_1 and x_2. The total scattered flux at θ_c is then,

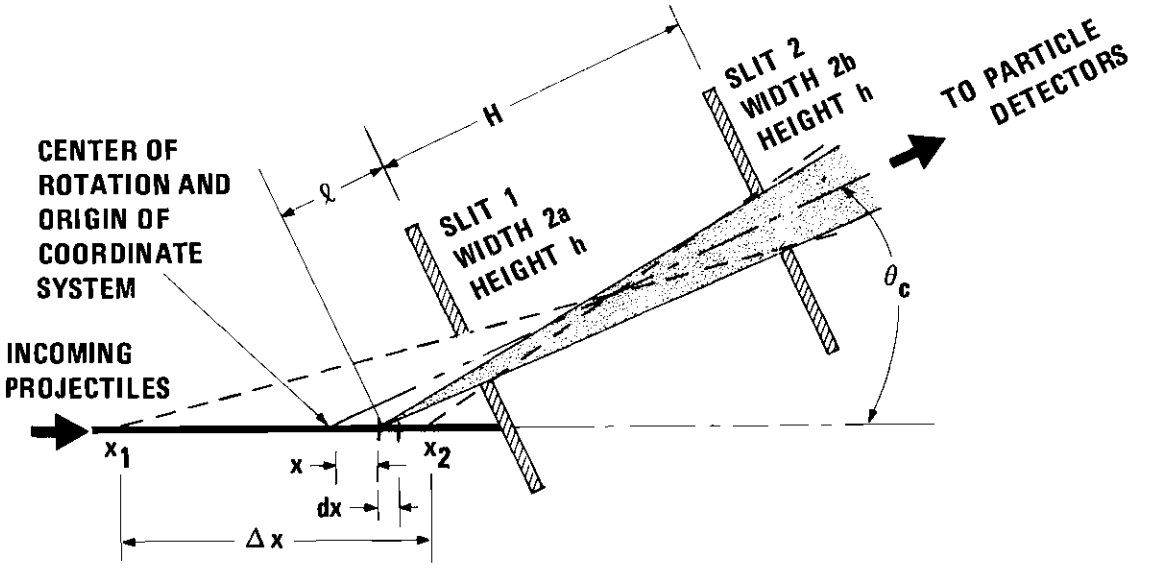

Figure 21. Schematic Diagram of Apertures Shown in the Plane that Includes the Incoming Beam and the Axis of the Apertures. Dimensions Used for the Analysis are as Follows: 2a = 0.0324 cm; 2b = 0.109 cm.; h_s = 0.31 cm.; ℓ = 4.17 cm.: H = 10.16 cm.

$$N_s(\theta_c) = \frac{N_B N_T}{A} \int_{\Delta\tau} \int_{\omega} I(\theta)\, d\Omega\, d\tau \quad . \tag{66}$$

The expression involves integration over the solid angle ω subtended by the apertures at some point in the beam path as well as integration over the total volume of the beam path $\Delta\tau$ that can be "seen" by the detectors through the apertures. It is clear, from Equation 66, that one cannot directly derive the true microscopic cross section, $I(\theta)$, from the measurement of scattered particle flux and other readily observable parameters. The usual procedure is to employ simplifying assumptions in order to remove an average $I(\theta)$ from the integral and thereby yield an approximation to the true value of cross section. One assumes the projectile beam to have negligible cross sectional area so that it is in effect a line, Equation (66) becomes,

$$N_s(\theta_c) = N_T N_B \int_{\Delta x} \int_{\omega} I(\theta)\, d\Omega\, dx \; . \tag{67}$$

It is then assumed the $\int_{\omega} I(\theta)\, d\Omega$ may be replaced by $I(\bar{\theta})\ \omega$; where ω is the solid angle subtended by the defining apertures at the target element dx and $I(\bar{\theta})$ is the value of the differential cross section at some angle $\bar{\theta}$ in the range encompassed by the solid angle. It is further recognized that the solid angle ω varies with the point on the beam path from which scattering occurs so that ω is a function of x. The equation (67) is thereby reduced to

$$N_s(\theta_c) = N_T N_B \int_{\Delta x} I(\bar{\theta})\ \omega(x)\, dx \tag{68}$$

Once again replacing the integral by $I(\bar{\bar{\theta}}) \int_{\Delta x} \omega(x)\, dx$ one arrives at

$$N_s(\theta_c) = N_B\, N_T\, I(\bar{\bar{\theta}}) \int_{\Delta x} \omega(x)\, dx \quad . \tag{69}$$

Finally, one assumes that the angle $\bar{\bar{\theta}}$, for which the cross section is appropriate, does in fact equal the nominal angle θ_c between the beam path and the geometrical axis of the defining apertures; that is to say $\bar{\bar{\theta}} = \theta_c$. Hence

$$N_s(\theta_c) = N_B\, N_T\, I(\theta_c)\, G(\theta_c) \tag{70}$$

where $G(\theta_c) = \int_{\Delta x} \omega(x)\, dx$. It is this last equation that is used to calculate cross sections from experimental data. Unless the assumptions made here are properly justified, comparison of an experimentally determined cross section with a theoretical prediction must be made with caution.

The calculation of the geometrical factor, $\int_{\Delta x} \omega(x)\, dx$, has already been considered a number of times for the particular case of two separate rectangular slits. Skalskaya[61] has shown how the integral may be calculated for this case. For reference Skalskaya's formula is reproduced here using the symbols given on Figure 21.

$$\int_{\Delta x} \omega(x)\, dx = \frac{a\, h_s}{H \cos \theta_c} \ln\left[\frac{2(H + \ell)\sin \theta_c + b \cos \theta_c}{2(H + \ell)\sin \theta_c - b \cos \theta_c}\right] \quad . \tag{71}$$

This formula assumes that the length of beam path observed by the detectors through the apertures does in fact lie entirely in the target region. At very small scattering angles the observed beam path may be very long and extend outside the region occupied by the target; in this case the formulation must be modified along the lines described

by Fillipenko.[57] Both formulations assume a line projectile beam and Fillipenko gives conditions under which a beam of finite size may be approximated by the line beam.

Now, we must address ourselves to three features of the problem. First, there is the influence of the aperture height on the calculation of the geometrical factor $\int \omega \, dx$. Secondly, there is the question of whether the cross section that one determines by insertion of experimental parameters into Equation (69) does, in fact, represent the cross section at the angle of the detection system θ_c; in simple terms the question of whether $\bar{\bar{\theta}}$ is approximately the same as θ_c. Finally, there is the question of how one should make comparison of a theoretical cross section with the apparent experimental value. In examples given throughout this discussion, we shall assume that the defining apertures are a pair of rectangular slits having the dimensions given in the caption of Figure 21. (This is one of two sets of apertures used in the present work.)

The Influence of Slit Height

In Figure 22, it is shown schematically a pair of rectangular apertures selecting particles scattered from a line beam at a point on the beam path coincident with the axis about which the apertures are rotated. The nominal angular setting of the apertures, θ_c, is customarily taken as the angle between the axis of the slits at their midpoint and the incoming direction of the particle beam. From Figure 22 it is obvious that particles scattered through the center of the slits have suffered an angular deviation θ_c. Those particles

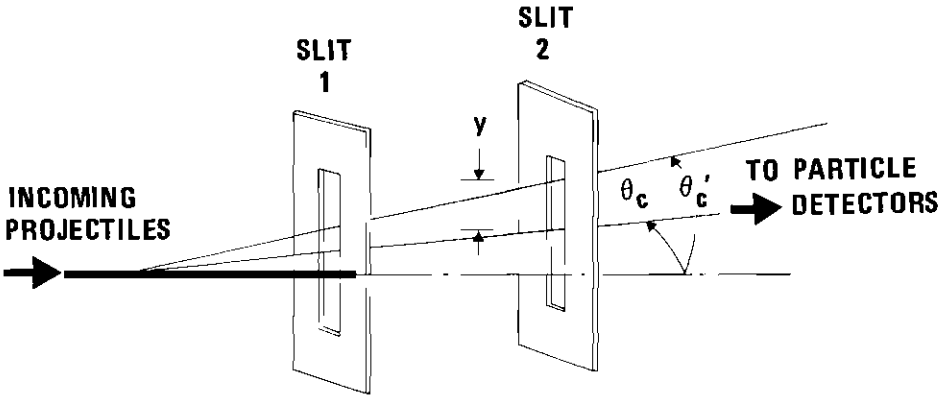

Figure 22. Three Dimensional Representation of Two Rectangular Defining Apertures.

scattered to some point at a distance y from the center of the second slit go through a slightly larger scattering angle θ_c' given by

$$\text{Tan } \theta_c' = \sqrt{\text{Tan}^2\theta_c + \left(\frac{y}{H + \ell}\right)^2} \quad . \tag{72}$$

The maximum value of θ_c^m, is found by replacing y by half the slit height $h_s/2$. The minimum value of θ_c' is the nominal angular setting θ_c. Figure 23 shows the variation of θ_c^m with θ_c for the particular case of the slit system described on Figure 21; that is to say, it shows the maximum scattering angle defined by the position of the apertures. Clearly, however narrow the slits, one does, in fact, accept a rather appreciable range of scattering angles and at small scattering angles the mean angle accepted is appreciably different from the nominal setting of the apertures. The range of angles accepted is, in fact, increased further when a beam of finite height is used since particles from the top of the beam scattered to the bottom of the slit goes through an angle greater than θ_c^m.

The first important conclusion from this is that the formulations of $\int\omega\, dx$ by Skalskaya[61] and by Fillipenko[57] are incorrect whenever there is an appreciable range of scattering angles encompassed by the height of the defining apertures. These two formulations were derived with a two-dimensional geometry described by Figure 21 and assume that scattering angles for particles exiting through the center of a slit are essentially the same as for particles exiting through the top of the slit. By Equation 72 this condition is met only when

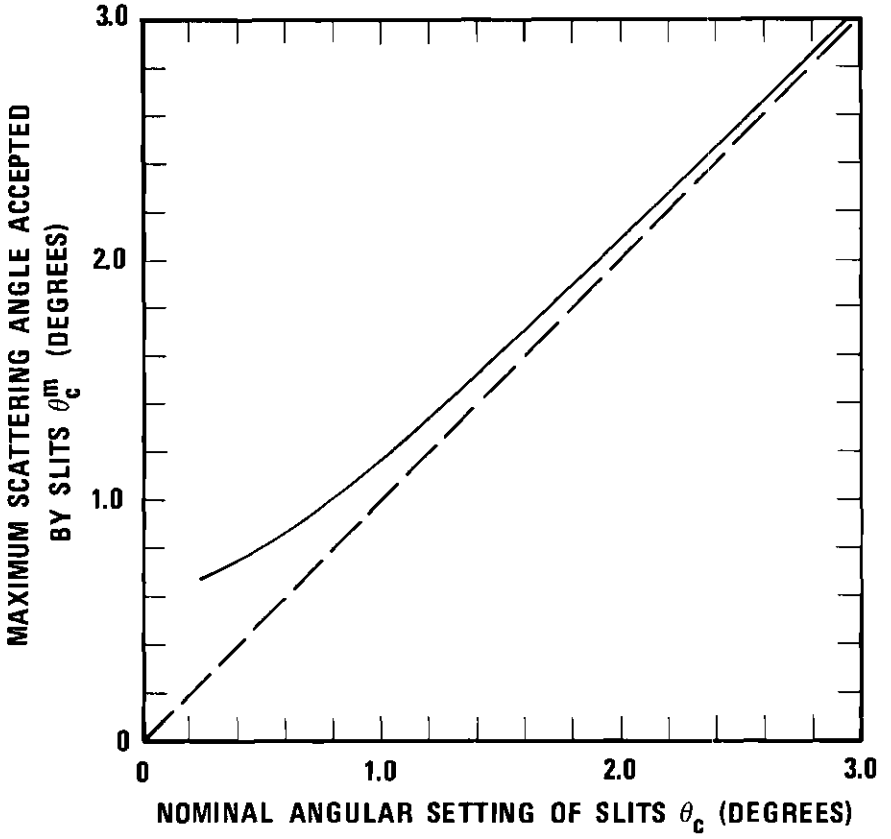

Figure 23. Maximum Scattering Angle Accepted by the Rectangular Aperture, θ_c^m, as a Function of the Nominal Angular Setting of the Apertures θ_c. The Solid Line is Calculated for the Geometry Shown in Figure 21. The Dashed Line would be Applicable for a Vanishingly Small Slit Height whereupon θ_c^m, = θ_c.

$$\left[\frac{h_s}{2}\,(H + \ell)\right]^2 << \mathrm{Tan}^2\,\theta_c \quad ; \tag{73}$$

for smaller angles the derived value of $\int \omega\, dx$ is incorrect.

The true value of $G(\theta_c)$ must be derived by numerical integration over the full height of the apertures. This may be achieved by segmenting the slit height into elementary parts, Δy, and using the equation of Skalskaya (Equation 71) to describe the contribution from that segment; the angle θ in Equation 71 must be separately chosen for each segment to represent the average angle through which particles must be scattered in order that they shall traverse this segment. The resulting expression is then integrated over the full slit height. The average value of the geometry factor is given by

$$G_{\substack{\text{averaged} \\ \text{over } h_s}}(\theta_c) = \frac{\int_{\theta_c}^{\theta_c^m} G(\theta_c')\, d\theta_c'}{\theta_c^m - \theta_c} \,. \tag{74}$$

Equation 74 was evaluated by using Equation 71 and performing the integration numerically* using Simpson's method. Figure 24 shows the calculated value $\int \omega\, dx$ using this integration over slit height. Also shown on that figure is a calculation of the geometrical factor for a beam of finite size with the dimensions of 0.1 cm height and 0.1 cm width. This was performed numerically by segmenting the beam into a series of strips that could be individually treated by the integral

---

*This numerical integration as well as all others discussed here was performed with sufficient iterations to tb within 0.1% of the true value and hence is not considered a source of error.

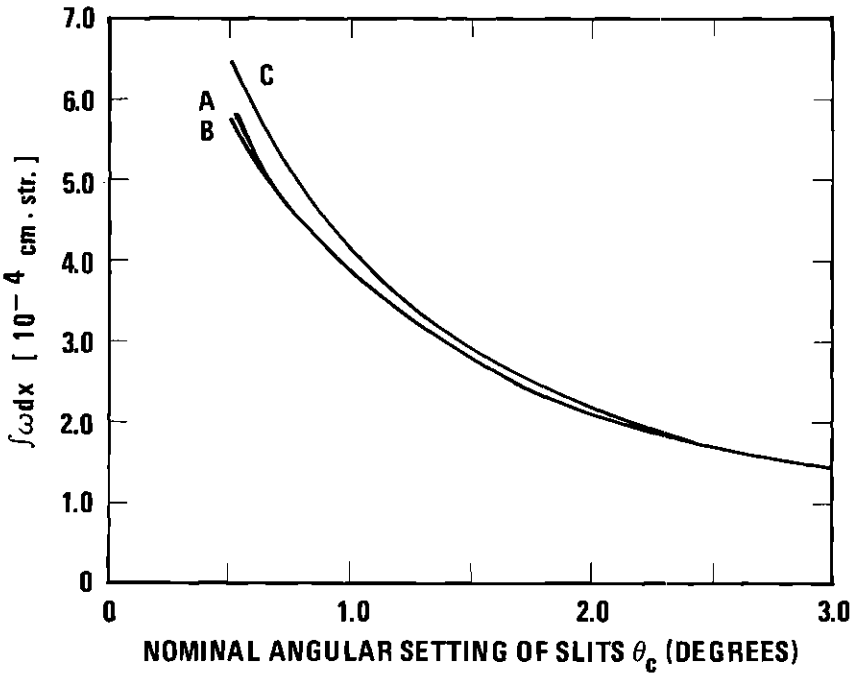

Figure 24. The Geometrical Integration Term $\int \omega \cdot dx$ Shown as a Function of the Nominal Angular Setting of the Apertures, θ_c. Curve A, Calculation Allowing for the Finite Slit Height and Employing an Average Over the Finite Size of the Incoming Projectile Beam (height 0.1 cm., width 0.1 cm.). Curve B, Calculation Allowing for Finite Slit Height but Neglecting Beam Size. Curve C, Calculation with Skalskaya's[61] Formula (Equation 71) that Neglects the Finite Size of the Projectile Beam and also Ignores the Distorting Effect of Slit Height.

$\int \omega\, dx$ which is evaluated at different values of b and then taking an average value over the full beam width. Incorporating the beam height into the evaluation of an average value of $G(\theta_c)$ requires segmenting the beam along the y direction and determining the range of θ_c 'seen' from each segment. Thus for some arbitrary point along the beam height y_B the extremes of θ_c is found from Equation 72 by replacing y with $h_s/2 \pm y_B$ where the + determines $\theta_c^{m_t}$, the maximum scattering angle defined by the top of the slit, and the - determines $\theta_c^{m_b}$, the maximum scattering angle defined by the bottom of the slit. Now the geometry factor averaged one beam width (w_B), beam height (h_B), and slit height (h_s) is

$$G_{AVG}(\theta_c) = \frac{\sin \theta_c}{h_B w_B} \int_{-h_B/2}^{h_B/2} \int_{\ell_{min}}^{\ell_{max}} \left[\frac{1}{\theta_c^{m_t} - \theta_c} \int_{\theta_c}^{\theta_c^{m_t}} G(\theta_c')d\theta_c' + \frac{1}{\theta_c^{m_b} - \theta_c} \int_{\theta_c}^{\theta_c^{m_b}} G(\theta_c')d\theta_c' \right] d\ell dy_b \qquad (75)$$

where $\ell_{\substack{max \\ min}} = \ell \pm w_B/2 \sin \theta_c$. Again, a numerical integration was performed by Simpson's method. It is this last calculation, involving both slit height and finite beam size that provides us with the true value of the integral that should be employed in the analysis of the experimental data. For comparison, Figure 24 also shows the calculation $\int \omega\, dx$ by the simple line formula of Skalskaya.[61]

It is clear from Figure 24 that the simple line integral without allowance for finite slit height and beam size is adequate for scattering angles of two degrees or more. At smaller angles, however, it is important to consider slit height: for the experimental parameters used here it can make a difference of 17% at one-half degree. The effect of finite primary projectile beam size is quite unimportant for our experimental arrangement.

Effective Angle of Scattering

It is now necessary to examine whether it is realistic to consider that the angular setting of the apertures is in fact the angle for which the differential cross section has been determined; that is to say, whether it is legitimate to set $\bar{\bar{\theta}} = \theta_c$ in proceeding from Equation 69 to Equation 70. The discussion of finite slit height, given above, indicates that a rectangular aperture will, in fact, accept a range of scattering angles. The nominal angular setting of the detection system defines the minimum scattering angle and certainly does not give the average scattering angle accepted by a detector system.

A further complication is seen in the consideration of the solid angle, $\omega(x)$, subtended by the apertures at some point x along the beam path. Figure 25 shows $\omega(x)$ as a function of x for various nominal scattering angles θ_c. If the shape of $\omega(x)$ had been triangular and centered about x = 0 (the axis of rotation of the detectors) then the approximation $\theta_c = \bar{\bar{\theta}}$ might be, in fact, reasonably accurate. It is apparent, however, that the curve of $\omega(x)$ is

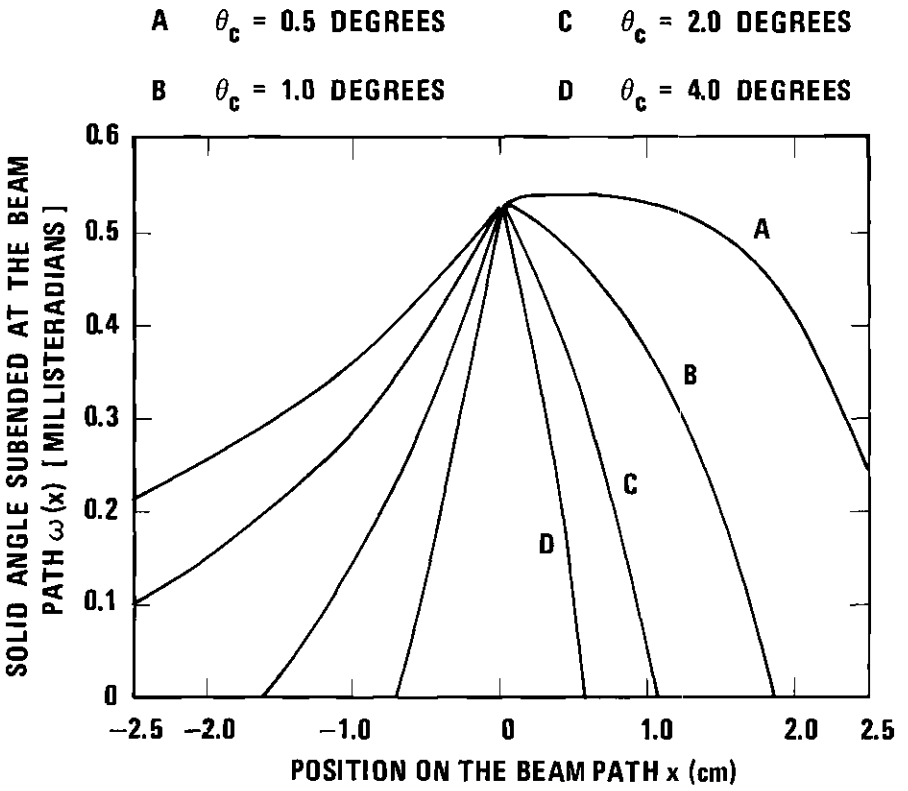

Figure 25. Graph of the Solid Angle $\omega(x)$ into which Particles are Accepted by the Apertures for Various Values of θ_c, Shown as a Function of the Beam Path, x, from which the Particles are Scattered.

certainly not triangular and, in fact, becomes increasingly skewed as smaller angles are approached. Figure 25 implies that at small angular settings the largest collection efficiencies are for position, down stream of the system's center (x = 0) and therefore involving larger scattering angles than the nominal setting of the detection system.

We have therefore two separate effects contributing to uncertainty in the angle $\bar{\bar{\theta}}$ for which the experimentally determined cross section is appropriate. Firstly, the finite slit height encompasses a range of scattering angles the average value of which is greater than the nominal angle of scattering defined by the collimating apertures. Secondly, the solid angle subtended by the slits at the beam path is not symmetrical about the axis of rotation for the aperture system so that the system is selective to projectiles scattered at some angle greater than the nominal angular setting of the apertures. The cumulative effect is that the angle, $\bar{\bar{\theta}}$, for which the measured cross section is appropriate, must be somewhat larger than the nominal angular setting of the apertures. If, as is generally the case, the cross section decreases with increasing scattering angle, than the measured cross section, $I(\theta_c)$, plotted as a function of the nominal scattering angle, θ_c, will lie below the true value of the cross section at that same angle.

It is clear that at sufficiently large scattering angles, there problems will tend to disappear and the measured cross section will approach the true value. At very small angles, however, the cross section derived by experimental measurement may be a considerable

distortion of the true value.

It must be admitted that the distortion of the cross section value could be much reduced by a choice of some other aperture arrangement. Instead of rectangular slits, one might employ annular ring apertures centered on the beam axis; this would transmit projectiles scattered into a cone and ensure that all transmitted particles were scattered at the same angle. There are, however, two practical drawbacks. Firstly, there would be severe mechanical problems in designing an annular system for which the scattering angle could be continuously varied in order to permit measurement of an angular distribution. Secondly, in order to detect the particles transmitted, one would need a rather large detector area; particle detectors of large sensitive area are not available. The problems associated with the variation of the solid angle, $\omega(x)$ with position along the beam path, x, would be alleviated by reducing the size of the first slit and so reduce the length of beam path that the detectors can observe. This has the disadvantage of reducing signals.

The relationship between $\bar{\bar{\theta}}$, the angle to which the measured cross section is appropriate, and θ_c the nominal angle that the apertures are set to transmit, is in fact, a function of the cross section as well as the geometrical parameters. To attempt derivation of a relationship between $\bar{\bar{\theta}}$ and θ_c would require some assumption as to the form of the cross section that one is attempting to measure. It is not the objective to carry out such an operation here.

The Comparison of Experimental Measurements with Theory

It is often the objective of experimental measurements to provide a test of a particular theoretical prediction. Given that the various distortions discussed above will occur, a question is raised as to how a comparison between theory and experiment can be made. Two approaches are possible. One may attempt to extract the true cross section from the measured distribution by a process of deconvolution. Alternatively the theoretical cross section may be mathematically convoluted into the experimental geometry to predict the cross section that should be measured by application of Equation 70.

There have been various discussions of deconvolution procedures that might be adapted for use in the present situation; there is, for example, the work of Moore.[58] Such procedures would, however, be useful only if the cross section is varying slowly over the range of angles accepted by the detector. In the event that the cross section were to oscillate rapidly with scattering angle, so that a number of oscillations were to be encompassed within the finite angular acceptance of the detector, then the measured cross section could not be deconvoluted to recover the true value. The problem is particularly severe when the experimental data exhibits statistical fluctuations. Thus, in general terms, deconvolution may not be the most satisfactory way of comparing theory and experiment.

The alternative technique is to take the theoretical predication of $I(\theta)$ and predict the value $I(\theta_c)$ that should be measured experimentally. By comparison of Equations (66) and (70)

$$I(\theta_c) = \frac{\int_{\Delta\tau} \int_{\omega} I(\theta)\, d\tau\, d\Omega}{A \int_{\Delta x} \omega(x)\, dx} \quad . \tag{76}$$

In performing both intergations, one needs to take into account the effect of slit height described in the earlier sections. The double integration in the numerator is performed in a manner analogous to that used in the determination $G(\theta_c)$, i.e., we assume a line beam (replace $\Delta\tau$ with $A\ \Delta x$), except that now the integration is performed numerically rather than analytically and the term, $d\Omega$, is now weighted by the differential cross section which we assume we know analytically. This double integral is then inserted into Equation (75) in place of $G(\theta_c)$ so that the finite beam and slit dimensions can be taken into account. To test that the computer program for performing this multiple integral was correct $I(\theta)$ was replaced by 1; this gave the correct value of $G(\theta_c)$, as it should have.

It is now interesting to consider a case in which experimental data had been compared with a theoretical prediction. Fitzwilson and Thomas using an apparatus similar to that described in Chapter II measured the differential cross sections for the two reactions

$$H^+ + He \rightarrow H^+ + He \tag{77}$$

and

$$H^+ + He \rightarrow H^o + He^+ \quad . \tag{78}$$

The detection geometry is identical to the one used for the present work. Their measurements for these two processes (at 10 keV impact energy) were summed together to yield the differential cross section

for cell scattering events resulting from H^+ impact on He. This cross section was then compared with a theoretical prediction by Bingham[59] that employs a "static potential" (see Chapter VI); this prediction takes into account all interactions between electrons and nuclei at all points during the collision process.

It was their original conclusion[29] that a systematic difference was exhibited between this theoretical calculation and the experimental data. The previously published data was re-evaluated using a corrected value for $\int \omega \, dx$ that takes into account the effects of finite slit height and projectile beam size in the manner discussed above. Figure 26 shows both the original published data as well as the corrected values. Also indicated on Figure 26, by curve A, is a prediction of this cross section by Bingham[59] using a static potential formulation. There is a substantial difference between the theory and the experimental values. A convolution was performed of Bingham's predictions into the experimental geometry using Equation (67); the result is curve B. Clearly, the convoluted cross section agrees with the corrected experimental data to within the accuracy of the original experimental data ($\pm$8%). One may thereby conclude that the theoretical predictions are completely consistent with the experimental data. The original comparison of uncorrected data with unconvoluted predictions did not support this conclusion. Then it can be seen that in order that a proper comparison between theory and experiment be made, the convoluted theory rather than the original theory should be used.

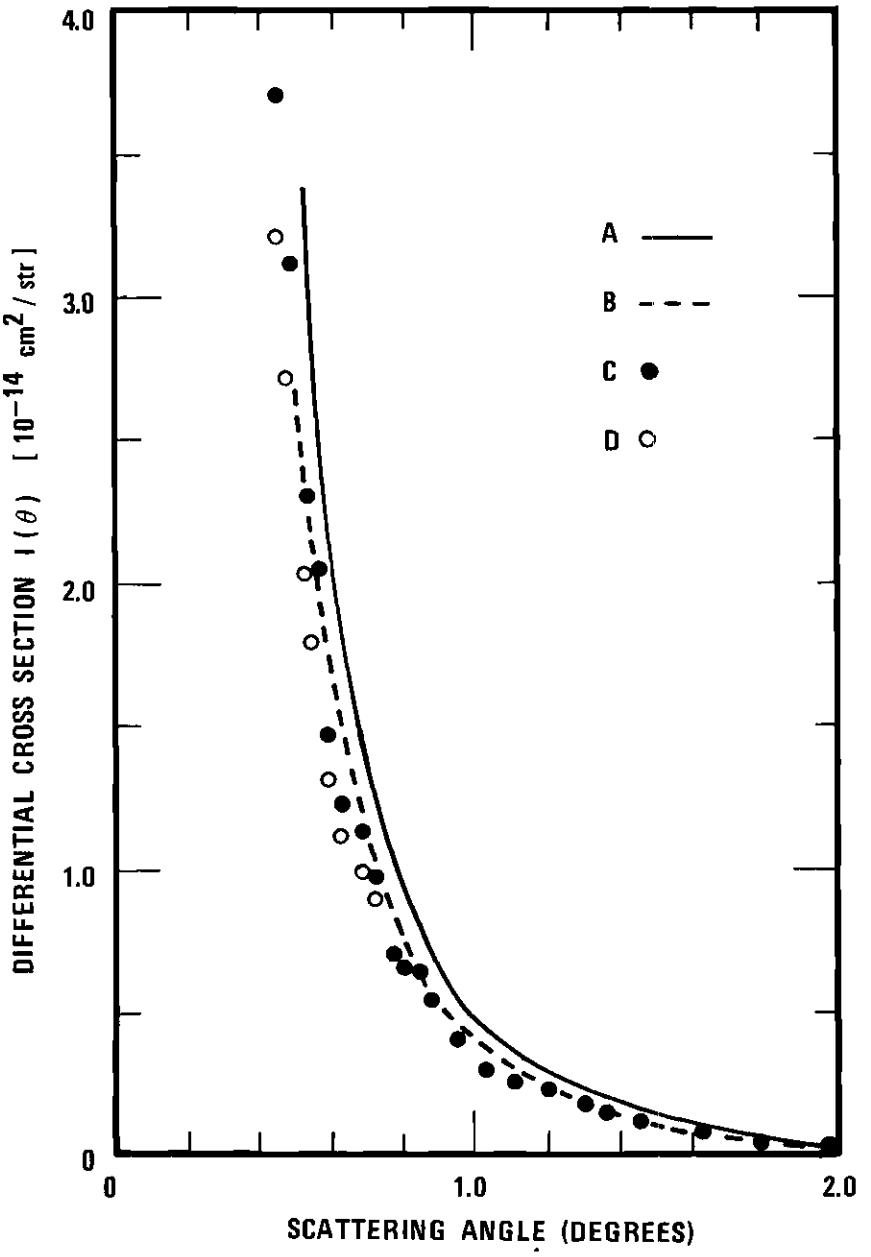

Figure 26. Cross Section for Scattering of all Particles (Protons and Neutral Hydrogen) Induced by 10 keV H^+ Impact on He. Curve A, Theoretical Calculation by Bingham[59]. Curve B, Predicted Result of Experimental Measurement Achieved by Convoluting Curve A into the Apparatus Geometry by the Use of Equation 75. Points C, Experimental Results Reanalyzed with a Geometrical Factor that takes into Account Finite Slit Height and Finite Beam Size. Points D, Experimental Data as Originally Published[29] Shown only where they Differ Significantly from the Corrected Points C.

REFERENCES*

1. E. W. Thomas, Excitation in Heavy Particle Collisions (Wiley-Interscience, John Wiley & Sons, Inc., New York, New York).

2. J. H. Montague, Phys. Rev. 81, 1126 (1951).

3. Ia. M. Fogel, V. A. Ankudinov, D. V. Pilipenko, and N. V. Topolia, J. Exptl. Theoret. Phys. 34, 579-592 [Soviet Phys. JETP 34, 400 (1958)].

4. G. W. McClure, Phys. Rev. 166, 22 (1967).

5. V. A. Ankudinov, E. P. Andreev, and A. L. Orbeli, Proc. 7th Int. Conf. on the Physics of Electronic and Atomic Collisions, Leningrad (Leningrad: Nauka), 312.

6. A. L. Orbeli, E. P. Andreev, V. A. Ankudinov, and V. M. Dukeskii, Zh. Eksperim.i Teor. Fiz. 57, 108 (1969) [Sov. Phys. JETP 30, 63 (1970)].

7. J. H. Birely and R. J. McNeal, Phys. Rev. A 5, 257 (1972).

8. R. H. Hughes and Suns-Sik Choe, Phys. Rev. A 5, 1758 (1972).

9. V. Dose, R. Gunz, and V. Meyer, Helv. Phys. Acta, 41, 269 (1968).

10. R. H. Hughes, H. M. Petefish, and H. Kisner, Phys. Rev. A 5, 2103 (1972).

11. D. R. Bates and G. W. Griffins, Proc. Phys. Soc. A66, 961 (1953); A67, 663 (1953); A68, 90 (1955).

12. D. R. Bates and A. Williams, Proc. Phys. Soc. A70, 306 (1957).

13. H. Levy II, Phys. Rev. 185, 185 (1969).

14. H. Levy II, Phys. Rev. 187, 136 (1969).

15. M. R. Flannery, Phys. Rev. 183, 231 (1969).

16. M. R. Flannery, Phys. Rev. 183, 241 (1969).

---

*Abbreviations used herein follow the form outlined in the Style Manual of the American Institute of Physics.

17. M. R. Flannery, J. Phys. B 2, 913 (1969).

18. R. H. Shields and J. L. Peacher, Phys. Rev. A 9, 743 (1974).

19. R. H. Shields and J. L. Peacher, Phys. Rev. A (To be published).

20. R. L. Fitzwilson and E. W. Thomas, Rev. Sci. Instr. 42, 1864 (1971).

21. J. N. Fox, R. L. Fitzwilson, and E. W. Thomas, J. of Phys. E = Sci. Instr. 3, 36 (1970).

22. E. W. Thomas, Excitation in Heavy Particle Collisions (Wiley-Interscience, 1972), Chapt. 9.

23. H. A. Bethe and E. E. Salpeter, Quantum Mechanics of One- and Two-Electron Atoms (Academic Press, Inc., New York, 1957).

24. S. Dushman, Scientific Foundations of Vacuum Technique (John Wiley & Sons, Inc., New York, 1962), second edition, p. 58.

25. L. H. Toburen, M. Y. Nakai, and R. A. Langley, The Measurement of High Energy Charge Transfer Cross Sections for Incident Protons and Atomic Hydrogen in Various Cases, Ph.D. Thesis of Toburen (Oak Ridge National Laboratory Report ORNL-TM-1988, 1967), p. 215.

26. E. S. Chambers, Phys. Rev. 133, A 1202, 1964.

27. P. M. Stier, C. F. Barnett, and G. E. Evans, Phys. Rev. 96, 973, (1954).

28. R. Dagnac, D. Blanc, and D. Molina, J. Phys. B3, 1239 (1970).

29. R. L. Fitzwilson and E. W. Thomas, Phys. Rev. A6, 1054 (1972).

30. E. P. Andreev, V. A. Ankudinov, and S. V. Bobashev, Soviet Phys. JETP 23, 375 (1966).

31. R. L. Fitzwilson, Ph.D. Thesis, Georgia Institute of Technology, August, 1971.

32. I. C. Percival and M. J. Seaton, Phil. Trans. Roy. Soc. (London), A251, 113 (1958).

33. Yardley Beers, Introduction to the Theory of Error (Addison Wesley Publishing Co., Inc., 1953), p. 33.

34. S. Dushman, Scientific Foundations of Vacuum Technique (John Wiley & Sons, Inc., New York, 1962), second edition.

35. Op. cit., Ref. 33.

36. D. H. Crandall, Thesis, University of Nebraska (1970).

37. I. A. Sellin, J. A. Biggerstaff, and P. M. Griffin, Phys. Rev. A2, 423 (1970).

38. D. Pretzer, B. Van Zyle, and R. Geballe, Phys. Rev. Letters 10, 340 (1963).

39. E. W. McDaniel, Collision Phenomena in Ionized Gases (John Wiley & Sons, Inc., 1964), p. 66.

40. Ibid., p. 75.

41. James K. Rice and Felton W. Bingham, Phys. Rev. A 5, 2134 (1972).

42. F. T. Smith, R. P. Marchi, W. Aberth, D. C. Lorents, and O. Heinz, Phys. Rev. 161, 31 (1967).

43. F. Herman and S. Skillman, Atomic Structure Calculations (Prentice-Hall, Englewood Cliffs, N. J., 1963).

44. E. H. S. Burhop, Quantum Theory I. Elements [edited by D. R. Bates], (Academic Press, Inc., New York, 1961), p. 379.

45. Ibid., p. 381.

46. Ibid., p. 378.

47. D. R. Bates, Atomic on Molecular Processes [edited by D. R. Bates], (Academic Press, Inc., New York, 1962), Chapt. 14.

48. T. J. Morgan, J. Geddes, and H. B. Gilbody, J. Phys. B 6, 2118 (1973).

49. J. L. Peacher, private communication.

50. Op. cit., Ref. 44, p. 381.

51. M. R. Flannery and K. J. McCann, Phys. Rev. A 8, 2915 (1973).

52. M. R. Flannery and K. J. McCann, To be published.

53. J. C. Y. Chen, C. J. Joachain, and K. M. Watson, Phys. Rev. A 5, 2460 (1972).

54. C. Bottcher and M. R. Flannery, J. Phys. B 3, 1600 (1970).

55. M. R. Flannery and K. J. McCann, Phys. Rev. A 8, 2915 (1973).

56. M. R. Flannery and K. J. McCann, To be published.

57. L. G. Fillipenko, Zh. Tekh, Fiz., 30, 57 (1960) Sov. Phys. Tech.] Phys. 5, 52 (1960).

58. L. Moore, Brit. J. Appl. Phys. (J. Phys. D.), Ser 2, 1, 237 (1968).

59. F. W. Bingham, private communications of a calculation performed by the method described in Phys. Rev. A., 5, 2134 (1972).

60. J. L. Peacher, private communication.

61. J. D. Skalskaya, Zh. Tekh. Fiz. 24, 1912 (1954). [Translated AEC--tr 2741].

VITA

Isidor Sauers was born in Linz, Austria on August 3, 1948. His parents, David and Nancy, are Polish emigrants who, after surviving Nazi concentration camp, resettled in the United States. Mr. Sauers was educated in Atlanta, where he attended Fulton High School followed by undergraduate and graduate work at the Georgia Institute of Technology. His undergraduate work was supported for four years by a Georgia Tech Alumni Fund Scholarship, while his graduate work was supported for one year by a teaching assistantship in the School of Mathematics, and for four years by a research assistantship in the School of Physics. He received the degrees Bachelor of Science and Master of Science in Physics in 1969 and 1970 respectively. He is a member of the honorary fraternity, Phi Eta Sigma, and the research society, Sigma Xi. He is also a member of the American Physical Society and has presented a paper to the Division of Electron and Atomic Physics at the Stanford Meeting of the APS in 1972.